Interannual Variability of Baiu Frontal Activity in May and its Connectivity with June

Tomita, Tomohiko

Yamaura, Tsuyoshi

(Citation)
Journal of the Meteorological Society of Japan. Ser. II,98(2):329-351

(Issue Date)
2020-04

(Resource Type)
journal article

(Version)
Version of Record

(URL)
https://hdl.handle.net/20.500.14094/90007235

Interannual Variability of Baiu Frontal Activity in May and its Connectivity with June

Tomohiko TOMITA

Faculty of Advanced Science and Technology, Kumamoto University, Kumamoto, Japan

and

Tsuyoshi YAMAURA

RIKEN Center for Computational Science, Kobe, Japan
Research Center for Urban Safety and Security, Kobe University, Kobe, Japan

(Manuscript received 14 April 2019, in final form 11 December 2019)

Abstract

The Baiu front (BF) is generally formed in May in the western North Pacific. Using objective analysis data from 1979 to 2014 (36 years), this study investigated the interannual variability of Baiu frontal activity (BFA) in May (BFA-M). In May, seasonal enhancement of warm and moist southerlies from the tropics climatologically establishes the BF as a large-scale quasi-stationary front. The strength of the southerlies from the tropics also controls the interannual variability of BFA-M. The anomalous large-scale circulation centered around Taiwan, which can be interpreted as a moist Rossby wave from the equatorial Kelvin–Rossby wave packet in the western tropical Pacific, modifies the strength of the southerlies. The equatorial Kelvin–Rossby wave packet, which is identified as the equatorial intraseasonal oscillation (ISO), propagates eastward from the Indian Ocean to the western Pacific.

The interannual variability of BFA-M has a biennial tendency, which stands in contrast with the three-year or four-year variation period of the El Niño/Southern Oscillation (ENSO). The biennial tendency is characterized by a zonal tripole distribution of sea surface temperature anomalies in the tropical Pacific, with corresponding anomalous Walker circulations. The induced anomaly fields are suitable for confining the disintegration of the equatorial Kelvin–Rossby wave packet in the western tropical Pacific and guiding the following northwestward propagation of the moist Rossby wave. With the phase reversal of ISO, the biennial tendency remains in the western part of the BF from May to mid-June, although the ENSO controls the BFA in the central part of the BF in June. This study proposes that the equatorial ISO in the Indian Ocean in April can be an indicator of BFA-M strength in the western North Pacific.

Keywords Baiu frontal activity in May; intraseasonal oscillation; biennial tendency; El Niño/Southern Oscillation

Citation Tomita, T., and T. Yamaura, 2020: Interannual variability of Baiu frontal activity in May and its connectivity with June. *J. Meteor. Soc. Japan*, **98**, 329–351, doi:10.2151/jmsj.2020-018.

Corresponding author: Tomohiko Tomita, Faculty of Advanced Science and Technology, Kumamoto University, Kumamoto 860-8555, Japan
E-mail: t-tomita@kumamoto-u.ac.jp
J-stage Advance Published Date: 11 February 2020

1. Introduction

The Meiyu/Baiu front is a subsystem of the East Asian summer monsoon, which yields a rainy season in early summer in East Asia and the western North Pacific. As a large-scale quasi-stationary front, the Meiyu/Baiu front is defined as a boundary between the northern and southern air masses in East Asia and the western North Pacific (e.g., Tomita et al. 2011). Because air masses are identified as having large-scale humidity and temperature homogeneity, a thermodynamic parameter, i.e., equivalent potential temperature, can detect the air mass boundary of the Meiyu/Baiu front (Tomita et al. 2011). The combination of the four air masses in East Asia and the western North Pacific may further divide the Meiyu/Baiu front in two by a meridian near 125°E, with the Meiyu front on the Asian continent and the Baiu front (BF) in the western North Pacific. The former is featured by a meridional gradient in humidity, whereas the latter is featured by a meridional temperature gradient. This study investigates the Baiu frontal activity (BFA) in May (BFA-M) in the western North Pacific by evaluating the precipitation rate in the BF.

The BF is usually established in May in the northwestern portion of the North Pacific subtropical high (Okada and Yamazaki 2012) and migrates northward with the subseasonal northward and westward expansion of this subtropical high until August (Murakami and Matsumoto 1994; Wang and LinHo 2002). Through numerical model experiments, Yoshikane et al. (2001) reported that large-scale thermal contrast between the ocean and the continent transformed zonally uniform atmospheric conditions, making the BF substantial. Kodama (1999) further found that the diabatic heating of tropical monsoons enhances the northeastward extension of the BF in numerical model experiments. Sampe and Xie (2010) demonstrated that westerly jet-induced horizontal temperature advection at 500 hPa determines the climatological location of the BF in June and July. There are many studies on the interannual variability of the BFA in June and July (e.g., Tanaka 1997; Tomita et al. 2004; Kosaka et al. 2011; Yamaura and Tomita 2011, 2014). Hereafter, we abbreviate Yamaura and Tomita (2011, 2014) as YT11 and YT14, respectively.

However, our understanding of BFA in its formative stage of May remains insufficient. In particular, there is a lack of understanding of the interannual variability of BFA-M and its connectivity with June. Okada and Yamazaki (2012) documented the climatological development of the BF in May and discussed the differences with its development in June, focusing on the horizontal temperature advection at 500 hPa. They found that unlike in June, in May the BF climatologically initiates with positive temperature advection from the south rather than from the west. Lau et al. (1998) and Tong et al. (2009) further indicated that the appearance of the BF in May coincides with the onset of the South China Sea (SCS) summer monsoon (SCS-SM). Wang and Xu (1997) elaborated that the climatologically fixed intraseasonal oscillation (ISO) determines the singularities of onset, breaks, and end of the Asian summer monsoon, which includes the BFA. Chen et al. (2000) revealed that the BFA had covariability with the monsoon trough zonally extending from the SCS to the western tropical Pacific through meridional circulations forced by tropical ISO disturbances.

Based on these earlier studies, we can summarize several points of discussion on the interannual variability of BFA-M as follows: (1) how anomalous environments modify the BFA-M, (2) the covariability between interannual BFA-M variation and the modulation of SCS-SM onset, and (3) the effects of ISO on the interannual BFA-M variation. Additionally, Tomita et al. (2010) reported that interannual anomalies of BFA tend to alternate from May to June, with anomalies in June able to remain until July due to effects of the El Niño/Southern Oscillation (ENSO). After a warm ENSO event, BF precipitation in May tends to be smaller, whereas precipitation in the following June and July is larger than usual. In addition to the three points above, we may further need to assess this change of interannual anomalies from May to June in more detail. YT14 already noted that the physical mechanisms in June and July are different, even if the polarity of the BFA anomalies remains unchanged from June to July after an ENSO event. Thus, the purpose of this study is to investigate the four points above and acquire a more comprehensive understanding of the interannual variability of BFA-M.

In the following Section 2, we provide an explanation of the data and methods used in this study. Section 3 briefly discusses the climatological development of the BF in May. Section 4 diagnoses the major factors controlling the interannual variability of BFA-M, focusing on ISO activity. Section 5 examines the connectivity of interannual BFA anomalies from May to June. Lastly, Section 6 provides a summary of this study as well as additional discussions. In this study, we define the interannual anomaly as the difference of each month or pentad from the climatological mean. Unless noted otherwise, seasons refer to seasons in the

Northern Hemisphere.

2. Data and methodology

This study uses three datasets: (1) the Global Precipitation Climatology Project (GPCP) (Adler et al. 2003), (2) the European Centre for Medium-Range Weather Forecasts Re-Analysis (ERA)-Interim (Dee et al. 2011), and (3) outgoing longwave radiation (OLR) edited by the U.S. National Oceanic and Atmospheric Administration (NOAA) (Liebmann and Smith 1996). The physical variable of GPCP is precipitation rate, with a unit of mm day^{-1}. The dataset covers 1979–2014 (36 years) with monthly temporal resolution and five-day means, the latter of which contains 73 pentads per year, and spatially covers the globe in a 2.5° longitude × 2.5° latitude grid. This study uses the isobaric surface parameters of the ERA-Interim dataset to examine large-scale atmospheric circulations and surface parameters such as sea surface temperature (SST), 2-m temperature, and 10-m horizontal wind to diagnose planetary boundary layer conditions. To equalize period and temporal resolution of the ERA-Interim with those of the GPCP, the original six-hour interval was re-edited as monthly and pentad means for 1979–2014 (36 years). The ERA-Interim dataset covers the entire globe with a horizontal resolution of 0.75° longitude × 0.75° latitude for 37 vertical pressure levels ranging from the surface to 0.1 hPa. The NOAA interpolated OLR dataset was used to examine ISO disturbances that are a major driver of tropical weather and climate (Madden and Julian 1994; Lawrence and Webster 2002). This study used the data from 1979 to 2014 (36 years) with daily intervals, which cover the entire globe with a 2.5° longitude × 2.5° latitude resolution.

We investigated the persistence of interannual BFA anomalies using cluster analysis, in which similarity among the interannual variations of sliding three-pentad means from early May to late June was evaluated for the Baiu precipitation rate. The time window length, i.e., three pentads or half a month, was used to remove high-frequency noise caused by synoptic-scale or smaller-scale disturbances. To measure the distance and evaluate the similarity, the cluster analysis employed the Ward method based on the Euclidean geometrical distance. The methodology is similar to that employed in YT14 except that the target period in YT14 was from early June to late July. Thus, this study may extend their target period to the entire Baiu season (i.e., early May to late July) to investigate the persistence of interannual BFA anomalies. Based on the results of YT14, we may more comprehensively understand the physical mechanisms involved in the interannual BFA anomalies at each stage of the entire Baiu season and the connectivity of those anomalies.

This study further employed composite and regression techniques to extract anomaly fields associated with the respective interannual BFA variations the cluster analysis identified. The climatological mean to calculate the anomaly was estimated using 1979–2014 (36 years) data. To isolate the ISO component, we applied a Lanczos band-pass filter (Duchon 1979) to the daily-mean data of each year, with the frequency response function set to be 0.5 at both ends of the 30–60–day periods. To highlight the biennial component, we also used a high-pass filter, i.e., $X_t - (X_{t-1} + X_{t+1})/2$, where X indicates the value of a physical variable in a specific year and t represents the year, which is termed a biennial filter in this study.

3. Climatology of the Baiu front in May

The BF climatologically forms in May, filling the blank between two ascending regions that appear in April, i.e., southeastern China and to the southeast of Japan (Figs. 1a, b). The increase in positive temperature advection at 500 hPa south of Japan induces a vertical direction change from downward in April to upward in May in this region, which corresponds to the seasonal development of warm moist southerlies from the tropics (Okada and Yamazaki 2012). BF convective activity is further enhanced during June, especially between 120°E and 140°E (Fig. 1c), with the increase in positive temperature advection due to westerlies at 500 hPa and the resultant increase of updrafts in the lower troposphere (Sampe and Xie 2010). We can perceive a northward shift of the BF from May to June between 120°E and 140°E (Figs. 1b, c).

The seasonal development of BF is also identified in the climatological distributions of May and June precipitation rates (Fig. 2). The thick solid contours in Figs. 2a, b indicate a climatological monthly mean precipitation rate of 5 mm day^{-1}, which can determine the climatological distribution of BF near Japan in May and June. The shading and thin contours in Figs. 2a, b represent the distributions of the mean precipitation rates and standard deviations of interannual variation, respectively. Vectors exhibit vertically (1,000–300 hPa) integrated water vapor fluxes (WVFs) that represent horizontal winds in the lower troposphere. The rectangle (125–145°E, 20–42.5°N) in each panel of Figs. 2a, b captures a core of the BF where the vertical flow changes from downward to upward in late spring (Figs. 1a, b). In this region, the northward shift of the BF occurs from May to June (Figs. 1b, c),

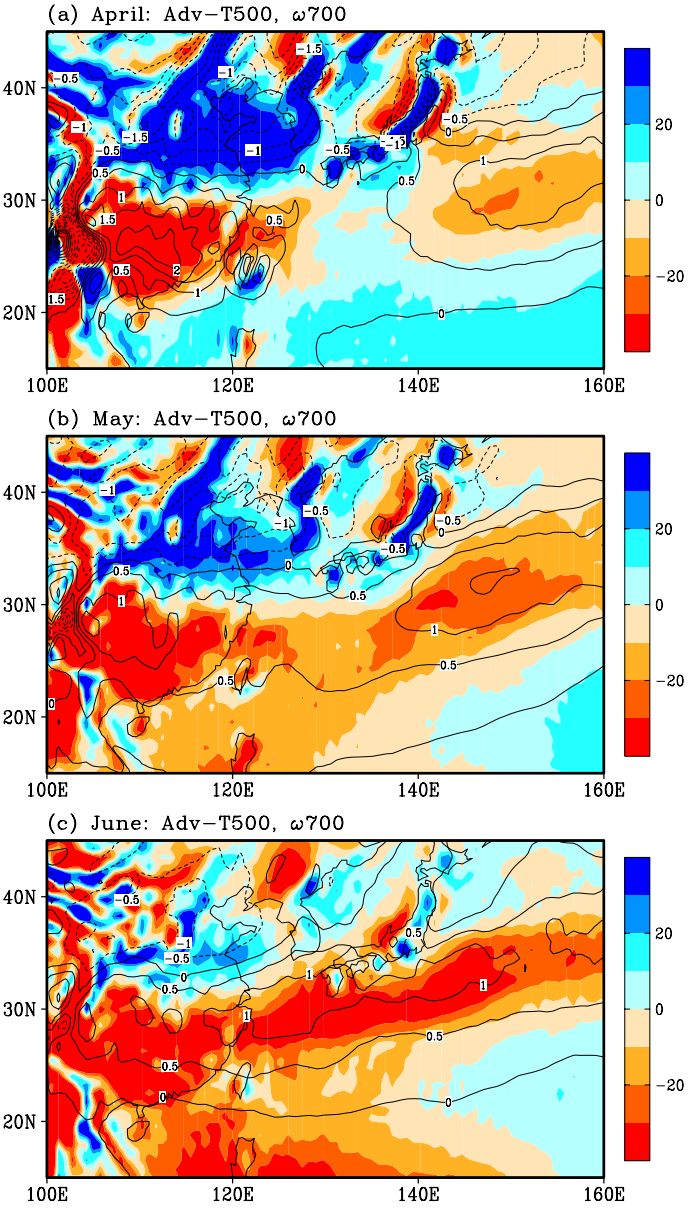

Fig. 1. Climatological (1979–2014, 36 years) monthly mean distributions of horizontal temperature advection at 500 hPa (contour; K day^{-1}) and vertical p-velocity at 700 hPa (ω700; color; hPa day^{-1}) in (a) April, (b) May, and (c) June. The contour interval is 0.5 K day^{-1}, and the dotted contours indicate negative values. Warm (cold) colors indicate ascent (descent), and the color scale is at the right of each panel.

and the interannual variation is large in both May and June (Figs. 2a, b). Figure 2c specifically shows that the BF moves northward from May to June between 125°E and 145°E with the modification of meridional circulation cells from the equator to 40°N. This study identifies the interannual variability of BFA before this northward shift.

To examine the climatological meridional shift of BF more precisely, we examined the time–latitude cross section of the pentad mean precipitation rates averaged from 125°E to 145°E (Fig. 3). The thick contours again indicate the precipitation rates of 5 mm day^{-1} and identify the meridional range of the climatological BF near 30°N. The lowest latitude thick contour determines the northern edge of the climatological intertropical convergence zone (ITCZ) from 125°E to 145°E. The shading and thin contours in Fig. 3 are like those in Figs. 2a, b. The three thin vertical lines designate the first days of May, June, and July and serve as monthly separations.

The BF climatologically develops on approximately May 10 near the Okinawa Islands in the western North Pacific (Fig. 3; Okada and Yamazaki 2012). The BF first expands southward at this time until late May,

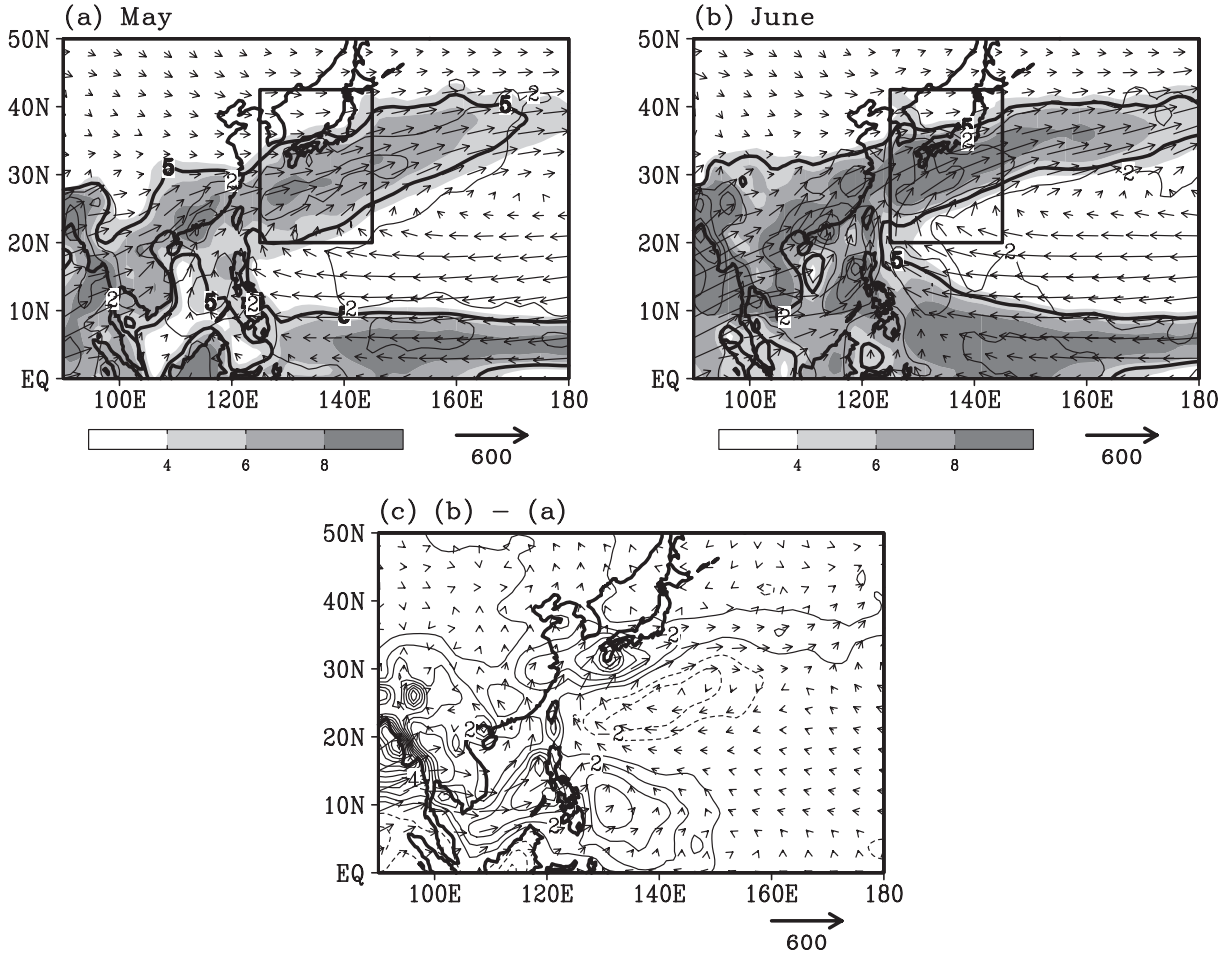

Fig. 2. Climatological (1979–2014, 36 years) monthly mean distributions of the precipitation rate (shade; mm day^{-1}) and vertically (1,000–300 hPa) integrated WVF (vector; kg m^{-1} s^{-1}) in (a) May and (b) June. The scales of the shading and vectors are at the bottom of each panel. Contours in (a) and (b) indicate the standard deviation of interannual precipitation rate variation with intervals of 2 mm day^{-1}. The zero contour is omitted for brevity. The thick solid contours in (a) and (b) indicate 5 mm day^{-1} in the climatological monthly mean precipitation rate, which identify the BF near Japan. The differences in precipitation rate (contour) and WVF (vector) between (a) and (b) (i.e., (b)−(a)) are shown in (c). The contour interval is 2 mm day^{-1}, and the dotted contours denote negative values. The zero contour is omitted for brevity. The scale vector is placed at the bottom. The rectangles in (a) and (b), i.e., 20–42.5°N, 125–145°E, is set to capture the center of the BF near Japan, where the climatological monthly mean of the precipitation rate and the interannual variation standard deviation are large.

with the precipitation rate increasing to 8 mm day^{-1} (shade) and the interannual standard deviation increasing to 6 mm day^{-1} (thin contour). Just before the appearance of the climatological BF, a disturbance with a large precipitation rate, which appears to be a phase-locked convective ISO disturbance, is observed between the equator and 10°N in early May. We will discuss the physical linkage between the appearances of the BF and the equatorial disturbances to the south in Section 4.

Even in April, the precipitation rate increases to 5 mm day^{-1} near 30°N, which may reflect the predominance of springtime mid-latitude cyclones. In fact, the large-scale frontal structure does not appear in middle tropospheric temperature advection and lower-tropospheric vertical motion fields near 30°N from 125°E to 145°E in April (Fig. 1a). In June, the southern and northern edges of BF both move northward at a speed

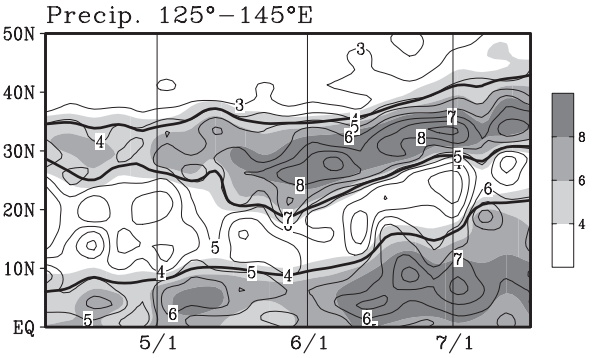

Fig. 3. A time–latitude cross section of the climatological (1979–2014, 36 years) mean precipitation rate averaged from 125°E to 145°E (shade; mm day^{-1}) and the interannual standard deviation (contour; mm day^{-1}) estimated from the pentad mean data. The shading scale is at the right and the contour interval is 1 mm day^{-1}. The contours at 5 mm day^{-1} for the mean precipitation rate are drawn as thick solid lines to highlight the latitudinal width of BF. Three vertical thin lines are drawn as borders between the months of April, May, June, and July.

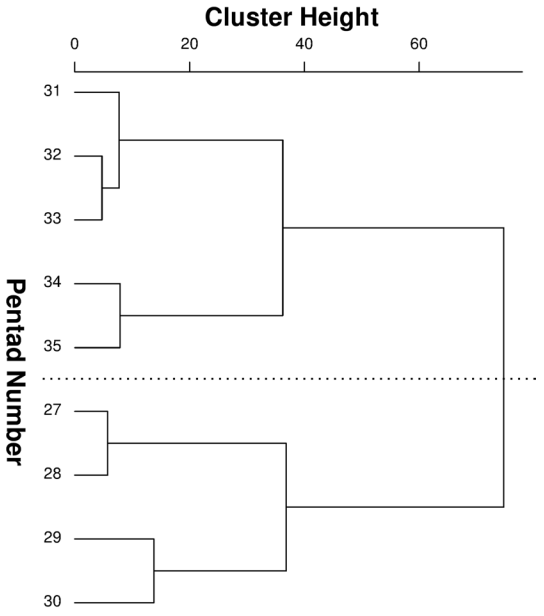

Fig. 4. Dendrogram of the cluster height for the pentad means in the precipitation rate from P27 (May 13) to P35 (June 22) in the rectangle region shown in Figs. 2a, b. The cluster heights are estimated based on the similarity between interannual variations of the pentad means, in which a simple three-pentad running mean was applied to eliminate components with synoptic and smaller scales. The time period from P27 (May 13) to P35 (June 22) is divided in two, i.e., P27–30 (May 13–28) and P31–35 (June 2–22).

of 5–10° month^{-1}, and the speed of the southern edge, i.e., ~ 10° month^{-1}, is twice that of the northern edge, i.e., ~ 5° month^{-1} (cf. Tomita et al. 2011). Therefore, the meridional width of the BF on June 1 (i.e., ~ 15°) narrows by approximately two-thirds (i.e., ~ 10°) by the end of June. We suggest that such northward BF movement belongs to the systematic modification of meridional circulation cells induced by the seasonal northward expansion of the ITCZ in the tropical western North Pacific. It is worth noting that northward climatological movement of the BF is gradual but not stepwise between 125°E and 145°E in June, despite northward expansion of the ITCZ being slightly stepwise (Fig. 3, shade). The features of climatological BF development in May and June may be summarized as follows: in May, the BF expands southward with increases in the precipitation rate and, in June, it gradually moves northward as it narrows.

4. Interannual variability of BFA-M and its controlling factors

In this section, we investigate the persistence of interannual BFA anomalies from May to June. In other words, identifying the controlling factors and how an anomalous BFA is maintained from May to June. To approach these issues, we first examine a cluster analysis dendrogram that measures similarities in interannual variations of the sliding three-pentad means of the Baiu precipitation rate, which are denoted by the boxes in Fig. 2 (Fig. 4). The temporal window length of the three pentads (i.e., 15 days) was used to evaluate the interannual variability in large-scale variations with periods longer than one week of the synoptic scale. The sliding three-pentad means can retain similar interannual tendencies in two continuous means as the two means have 10-day periods that overlap. In Fig. 4, the pentad numbers derive from the center of three continuous pentads. Hereafter, the pentad number, which is ordered from 1 to 73 in a year, is expressed by the combination of P and the number of the pentad (e.g., P30), and the central date of the pentad is additionally shown to improve understanding (e.g., May 28).

A large discontinuity was detected between P30 (May 28) and P31 (June 2) in terms of similarity in the

interannual variability of the Baiu precipitation rate (Fig. 4). The two divided clusters, i.e., P27 (May 13) to P30 (May 28) and P31 (June 2) to P35 (June 22), represent the periods during which similar interannual tendencies continue in Baiu precipitation rates. In this cluster analysis, we determined the beginning of the former period based on the timing of southward BF expansion and increases in the Baiu precipitation rate (Fig. 3). Meanwhile, we determined the end of the later period based on the findings of YT14, in which they found the next discontinuity between P35 (June 22) and P36 (June 27). YT14 identified two physical mechanisms in June and July, both of which were attributed to ENSO through different processes. However, YT14 did not discuss the interannual variability of BFA-M and its connectivity with that in June.

Figure 5 shows the interannual variations of the Baiu precipitation rate in the rectangle region shown in Fig. 2 (Fig. 5a) and their power spectral densities (Figs. 5b, c), which were estimated from the two time means from P27 (May 13) to P30 (May 28) (solid; IDX1) and from P31 (June 2) to P35 (June 22) (dashed; IDX2). The former time series, i.e., IDX1, represents the interannual variability of BFA-M, whereas the latter time series, i.e., IDX2, indicates the interannual variation of the BFA in June. The correlation coefficient between IDX1 and IDX2 is 0.13, and the correlation is statistically insignificant. Additionally, the dominant interannual periodicity differs between these time series, i.e., 2.5 years per cycle for IDX1 in May (Fig. 5b) and 2.3 and 3.3 years per cycle for IDX2 in June (Fig. 5c). The difference in dominant periodicity may explain the weak correlation, further suggesting that the major forcing mechanisms differ between May and June. This study focuses on the physical mechanisms in May because YT11 and YT14 have already examined the mechanisms occurring in June. However, both IDX1 and IDX2 demonstrate an interdecadal modulation near 1994 (Fig. 5a), which yields a change from lower to higher frequencies. This issue is a topic for future study.

Table 1 summarizes the correlations of IDX1 and IDX2 (Fig. 5) with several ENSO indices in antecedent winter and spring, the ENSO Modoki (Ashok et al. 2007) in spring (also called the central Pacific ENSO) (cf. Feng et al. 2015; Pang et al. 2016), and the indices of BFA in June (YT11 and YT14). Additionally, we estimated the correlation with the interannual variation of SCS-SM onset date, which was estimated using ERA-Interim data through the definition of Wang et al. (2004). The ENSO Modoki index is characterized by a tripole distribution of SST anomalies (SSTAs) in the

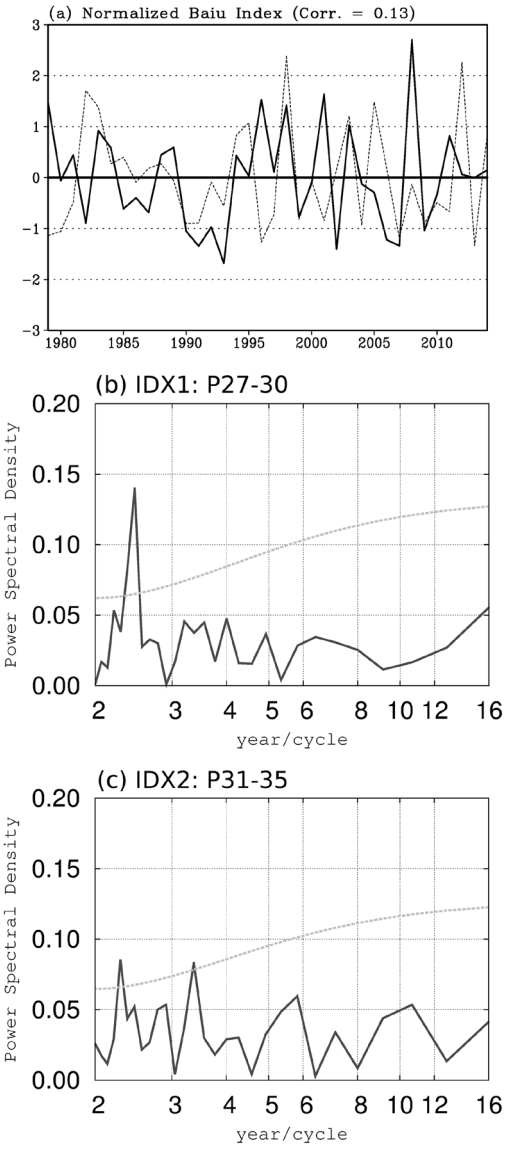

Fig. 5. (a) Normalized time series of precipitation rates in the rectangle region shown in Figs. 2a, b and (b and c) their power spectral densities. Only data in the areas that cover the 5 mm day^{-1} or more for the mean and 2 mm day^{-1} or more for the standard deviation in the rectangle region were averaged. The solid line values in (a) were estimated from the mean precipitation rate for P27–30 (May 13–28) (referred to as IDX1), whereas those for the broken line in (a) were from the mean precipitation rate for P31–35 (June 2–22) (referred to as IDX2). In (b and c), the dashed line indicates statistical significance at the 5 % level for the power spectral densities, which were estimated from the red noise spectrum based on a first-order autoregression.

Table 1. Correlation coefficients for the Baiu frontal activity (BFA) indices, i.e., IDX1 in May (P27–30) and IDX2 in June (P31–35), with the El Niño Southern Oscillation (ENSO) indices of the area mean SSTA in NINO1+2 (0–10°S, 90–80°W), NINO3 (5°N–5°S, 150–90°W), NINO4 (5°N–5°S, 160°E–150°W), and NINO West (0–15°N, 130–150°E), with the ENSO Modoki index of SSTA(A) − (SST(B) + SST(C))/2, in which A is 165°E–140°W, 10°S–10°N, B is 110–70°W, 15°S–5°N, and C is 125–145°E, 10°S–20°N, with the BFA indices in June from previous studies, i.e., the Early Baiu (YT14), Western Baiu (YT11), Central Baiu (YT11) and the index for the South China Sea summer monsoon (SCS-SM) onset day defined by Wang et al. (2004), which has been extended to 2014 using the ERA-Interim dataset. The bold numbers indicate correlation coefficients that are statistically significant at the 5 % level.

	IDX1 (P27–30)	IDX2 (P31–35)
NINO1+2 (DJF)	+0.19	**+0.49**
NINO3 (DJF)	+0.03	**+0.42**
NINO4 (DJF)	−0.24	+0.18
NINO West (DJF)	+0.31	−0.23
NINO3 (MAM)	−0.07	+0.33
NINO4 (MAM)	**−0.37**	+0.18
NINO West (MAM)	+0.29	−0.28
Modoki (MAM)	**−0.50**	−0.04
Early Baiu	+0.13	**+0.79**
Western Baiu	**+0.41**	−0.00
Central Baiu	−0.02	**+0.82**
SCS-SM onset	−0.32	−0.06

tropical Pacific (Ashok et al. 2007), in contrast with the seesaw-like dipole of ENSO (e.g., Rasmusson and Carpenter 1982).

IDX2 well represents interannual BFA variability in June. In fact, the correlations with other BFA indices in June, i.e., the indices of Central Baiu in YT11 (0.82) and of Early Baiu in YT14 (0.79), are quite strong (Table 1). Additionally, the interannual BFA variability in June correlates with the ENSO indices. In particular, the correlation coefficients are significantly positive for the antecedent winter indices, i.e., NINO1+2 (0.49) and NINO3 (0.42), in the eastern-central tropical Pacific (Table 1). In this study, we evaluated the statistical significance using two tailed t-test, with the degree of freedom set to 34, and the estimated correlation coefficients were ±0.34 at the 5 % level. Negative correlations with NINO West in antecedent winter (−0.23) and spring (−0.28) reflect the east-west seesaw-like SSTA variation in the tropical Pacific occurring in the ENSO (Table 1). The correlations between IDX2 and spring ENSO indices are generally weak, although similar positive and negative correlation tendencies continue from winter to spring (Table 1). YT11 and YT14 attempted to understand the spatiotemporal details of interannual BFA variations in June and July, and identified two controls of ENSO through the Pacific–East Asian teleconnection (Wang et al. 2000) and the capacitor effect of the Indian Ocean (Xie et al. 2009).

For May, IDX1 has significant correlations with indices of NINO4 in spring (−0.37), the ENSO Modoki in spring (−0.50), and the Western Baiu in June (0.41, YT11), all of which are statistically significant at the 5 % level. Based on these significant correlations, we examine the physical mechanisms and environmental conditions that control interannual variability of IDX1 in May with connectivity to June. Additionally, we account for the correlation with the interannual variation of SCS-SM onset day (−0.32; Wang et al. 2004), although this correlation is slightly weak and not statistically significant at the 5 % level. Paradoxically, we may need to understand the reasons why IDX1 in May does not correlate with IDX2 in June, the ENSO indices in the central-eastern tropical Pacific (NINO1+2 and NINO3), and the major Baiu indices in June, i.e., the Early and Central Baiu (Fig. 5; Table 1).

Figure 6 shows anomaly fields for precipitation rate (contour) and vertically (1,000–300 hPa) integrated WVF (vector) associated with IDX1 and IDX2 (Fig. 5a). The interannual anomalies in May (P27–30; Fig. 6a) are characterized by both an anomalous cyclonic circulation centered near Taiwan and positive precipitation rate anomalies expanding northeastward from the center, which reflect a stronger-than-usual BFA-M. Hereafter, this anomalous cyclonic circulation is referred to as the control circulation of BFA-M (CCBM). As part of CCBM, anomalous westerlies are observed in the central SCS, i.e., 100–130°E and 0–15°N, and positive precipitation rate anomalies appear in the northern part of the region containing westerly anomalies. These anomalies in the central SCS are probably related to the onset of SCS-SM or indicate its active phase in May (Lau et al. 1998; Chen et al. 2000; Wang et al. 2004; Mao and Chan 2005). In fact, the climatological onset date of SCS-SM is May 20, though this date can range from early May to early June (Wang et al. 2004; Wang et al. 2018). We can observe specific zonal wind anomalies in the equatorial region in May (Fig. 6a), i.e., westerlies in the eastern Indian Ocean and easterlies in the western Pacific.

Interannual anomalies in June (P31–35; Fig. 6b) can be represented by anomalous southwesterlies

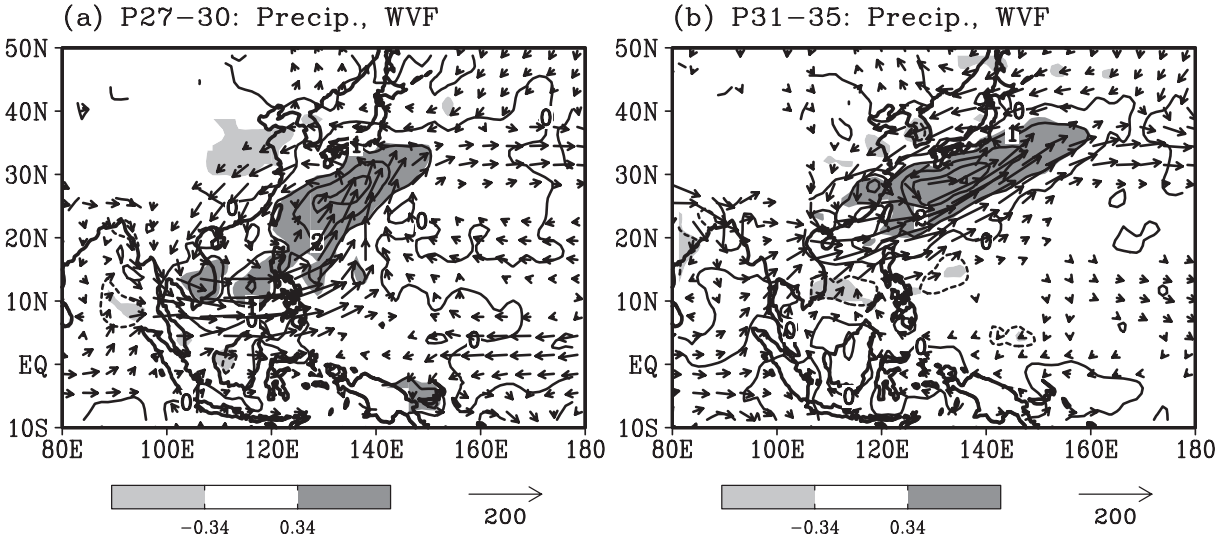

Fig. 6. Anomalies for precipitation rate (contour; mm day^{-1}) and vertically (1,000−300 hPa) integrated WVF (vector; kg m^{-1} s^{-1}) estimated from the regression coefficients based on (a) IDX1 in May (P27−30) and (b) IDX2 in June (P31−35) in Fig. 5a. In both (a) and (b), the contour interval is 1.0 mm day^{-1} and dashed contours indicate negative anomalies. Dark (light) shaded regions are statistically significant at the 5 % level, which are determined from the positive (negative) correlation coefficients for (a) IDX1 or (b) IDX2 (±0.34, in which the degree of freedom (d.f.) was estimated as 34). The scale vector is at the bottom right of each panel, and vectors smaller than 1/20 of the scale vector are omitted for brevity.

from the northern SCS to the western North Pacific and opposite anomalous northeasterlies to the north that form an elliptical northeastward-extending cyclonic circulation south of Japan. We observe positive Baiu precipitation rate anomalies in this anomalous cyclonic circulation where warm and humid monsoon air converges. We can also obtain negative precipitation rate and anticyclonic circulation anomalies surrounding the Philippines. YT11 and YT14 reported on interannual BFA variability in June with a meridional dipole structure of anomalous anticyclonic and cyclonic circulations like that shown in Fig. 6b, and discussed the physical mechanisms following ENSO (Table 1).

Interannual variability of BFA-M correlates with the tripole SSTA pattern that appears in the tropical Pacific in the preceding winter, which is similar to the pattern seen in ENSO Modoki (Fig. 7a). In the tripole pattern, significant positive (negative) SSTAs appear in the tropical western (central) Pacific, much like the La Niña Modoki SSTA field. Thus, when SSTAs are positive in the Philippine Sea in the earlier winter, the BFA-M tends to be strong. In contrast, when the interannual BFA anomalies in June are large, a dipole SSTA pattern occurs in the tropical Pacific in the preceding winter (Fig. 7b), which corresponds to that of a conventional El Niño (Table 1). The Baiu precipitation rate tends to be larger than usual in June after an El Niño event (Tanaka 1997, among others). YT14 extensively described the physical processes from the earlier winters of ENSO warm event to June in the Baiu season. Interestingly, tropical Pacific SSTA distributions have a quadrature phase relationship between Figs. 7a and 7b; i.e., the positive and negative SSTA maxima in Fig. 7a appear near the zero lines between the large positive and negative SSTAs in Fig. 7b. This spatial quadrature phase relationship further supports the insignificantly weak correlation between IDX1 and IDX2 (0.13; Fig. 5a). Hereafter, we focus on the anomaly fields associated with the interannual variability of BFA-M represented by IDX1 (Figs. 5a, b). We examine 1) the formation of the CCBM in May (Fig. 6a), 2) the tripole SSTA pattern in the tropical Pacific from the previous winter (Fig. 7a), and 3) their relationship.

We can identify the time development differences between the strong and weak cases with the time–latitude cross sections of precipitation rate (contour) and a proxy of lower-tropospheric horizontal winds (vector) (Figs. 8a, b), averaged from 125°E to 145°E in the BFA-M core region (Fig. 2). These are similar to those for climatology shown in Fig. 3, but with ver-

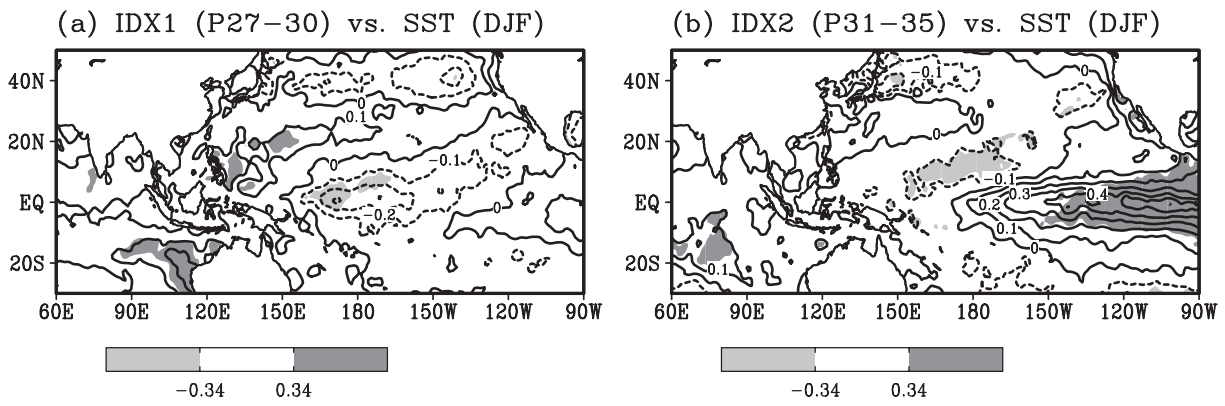

Fig. 7. SSTAs estimated from the regression coefficients between the preceding winter (DJF) mean SST and (a) IDX1 in May (P27−30) or (b) IDX2 in June (P31−35). In both (a) and (b), the contour interval is 0.1 K and the dashed contours indicate negative anomalies. Dark (light) shaded regions are statistically significant at the 5 % level, which are determined from the positive (negative) correlation coefficients with (a) IDX1 or (b) IDX2 (±0.34; d.f. = 34).

tically (1,000−300 hPa) integrated WVF. These values are simply estimated from an average of positive (Fig. 8a) or negative (Fig. 8b) years in the IDX1 time series (Fig. 5a). Additionally, Fig. 8c shows the difference between the strong and weak cases.

For the strong BFA-M (Fig. 8a), the thick 5 mm day^{-1} contour indicates that the southern boundary of the BF reaches 20°N by May 10, with an appearance of a precipitation rate greater than 7 mm day^{-1} in the BF. We also see an increase in southerlies near the southern BF boundary near 20°N. A transient precipitation event occurs from 0° to 10°N in early May just before the southward expansion of BF. This equatorial precipitation event remains for 10−15 days from the beginning of May, suggesting that the event is due to convective ISO disturbances. In June, the BF gradually moves northward at approximately 10° month^{-1} as it narrows, during which time the ITCZ concurrently expands northward as it intensifies. From early May to the middle of July, we find several stepwise northward shifts or northward protrusions with the gradual northward expansion of the ITCZ.

For the weak BFA-M (Fig. 8b), the southward expansion of the BF in May is delayed by approximately 15 days compared the strong case (Fig. 8a). Concurrently, the increase in southerlies is also delayed near the southern boundary of the BF near 20°N. Around May 10, a northward intrusion of small precipitation rates occurs near 25°N. The equatorial precipitation event is weaker and delayed by approximately 5 days compared with the strong case (Fig. 8a). During the first half of July, the weak case precipitation rate (Fig. 8b) is greater than that in the strong one (Fig. 8a) from the tropics to mid-latitude.

Figure 8c shows differences between the strong and weak cases (strong – weak). First, the precipitation rate differences are temporarily large in May at 17−32°N associated with the strengthening of southerlies there. Second, a small anomalous precipitation event occurs in the equatorial region in early May. Third, in June, a northward deflection of the BF is identified in the strong case due to an anomalous meridional dipole in the precipitation rate with a northern positive anomaly with westerlies and a southern negative anomaly at 20−37°N. Fourth, in the first half of July, the precipitation rate south of 42°N is generally smaller in the strong case than in the weak case.

The development of the CCBM in May (Fig. 6a) can cause southward expansion of the BF and strengthen southerlies to the south during May (Fig. 8). We examine growth and decay of CCBM in more detail by applying a regression technique based on IDX1 (Fig. 5a) to a weighted, i.e., (1, 2, 1)/4, three-pentad mean fields of precipitation rates and vertically (1,000−300 hPa) integrated WVFs (Figs. 9, 10). To extract components larger than the synoptic scale, we used the weighted three-pentad mean. Figure 9 shows the growth stages of CCBM. At around P25 (May 3; Fig. 9a), small southerly wind anomalies and small positive precipitation rate anomalies appear south of Japan between 120°E and 140°E. There are no prevailing westerly anomalies over the central SCS during this stage. Over the Indonesian maritime continent, we identify the confluence of anomalous westerlies in the

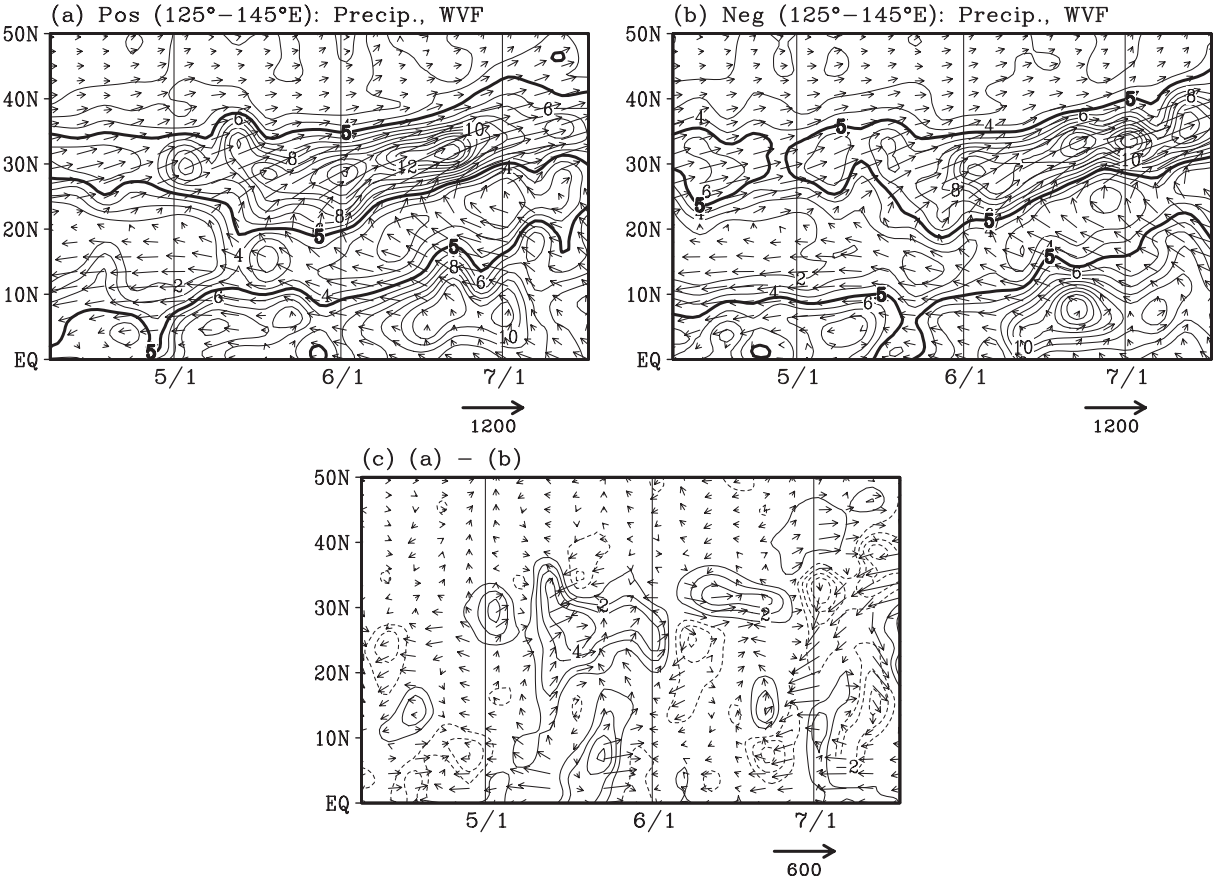

Fig. 8. Time–latitude cross sections of the precipitation rate (contour; mm day^{-1}) and vertically (1,000–300 hPa) integrated WVF (vector; kg m^{-1} s^{-1}) averaged from 125°E to 145°E for approximately three months from mid-April to mid-July for (a) positive and (b) negative years in IDX1 in Fig. 5a. The values were estimated from the averages of positive and negative years in the IDX1. The contour interval is 1 mm day^{-1}, and the scale vector is at the bottom right. Thick solid contours indicate 5 mm day^{-1}, and highlight the meridional range of the Baiu front (BF) and the northern edge of the intertropical convergence zone (ITCZ) from 125°E to 145°E. The differences (i.e., (a)−(b)) are shown in (c). In (c), the solid (dashed) contours denote the positive (negative) values with intervals of 1 mm day^{-1} without the zero contours. The scale vector is at the bottom right.

eastern Indian Ocean and anomalous easterlies in the western Pacific.

By P26 (May 8; Fig. 9b), the anomalous southerlies are enhanced with an increase in positive precipitation rate anomalies south of Japan. Concurrently, we observe the enhancement of the North Pacific subtropical high and strengthening of the equatorial confluence between 120°E and 140°E. The appearance of anomalous westerlies in the central SCS probably reflects an early onset of the SCS-SM (e.g., Wang et al. 2018). A similar situation remains until P27 (May 13; Fig. 9c), with the formation of closed CCBM (Fig. 6a). The positive precipitation rate anomalies then increase in the southern part of BF in May and extend to the south (Fig. 8a). The CCBM persists until P28 (May 18; Fig. 9d), with strengthening of the anomalous northeasterlies in the northwestern part of the BF while the North Pacific subtropical high weakens.

Decay of the CCBM begins to occur around P29 (May 23; Fig. 10a), with an eastward shift of the confluence of the anomalous equatorial zonal winds to 155°E. By P30 (May 28; Fig. 10b), the CCBM is further weakened, with a decrease in positive Baiu precipitation rate anomalies. By P31 (June 2; Fig. 10c) the anomalous westerlies become easterly wind anomalies surrounding the Philippines, and an anomalous anticyclonic circulation is formed southeast of Japan. Until P32 (June 7; Fig. 10d), the easterly wind

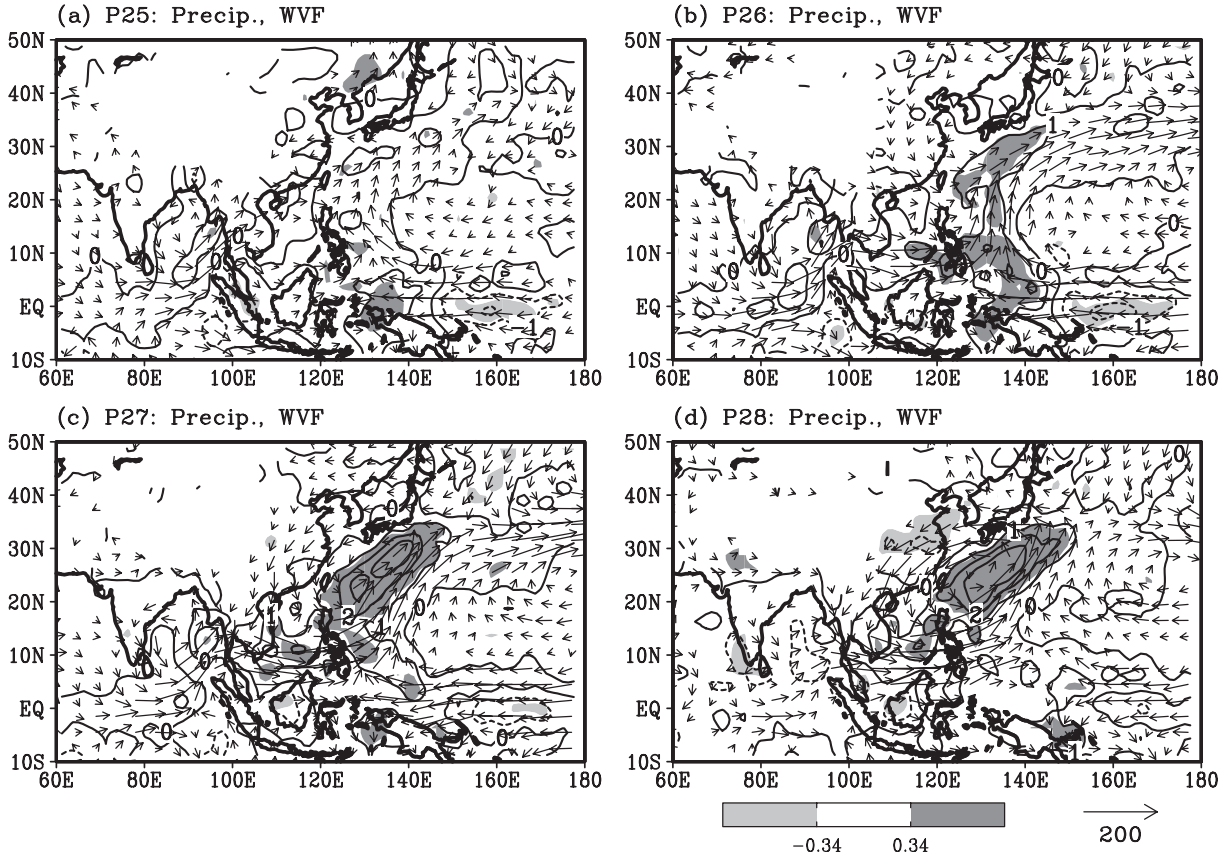

Fig. 9. Spatiotemporal development of the anomalous circulations that activate the Baiu frontal activity in May (BFA-M). The time period is from P25 to P28, i.e., (a) P25 (May 3), (b) P26 (May 8), (c) P27 (May 13), and (d) P28 (May 18). A (1, 2, 1)/4 weighted three-pentad mean was used to smooth out the high-frequency components with periods of less than 15 days. Contours indicate precipitation rate anomalies (mm day^{-1}) with intervals of 1.0 mm day^{-1}. Dashed contours indicate regions with negative anomalies. Vectors denote the vertically (1,000–300 hPa) integrated WVF (kg m^{-1} s^{-1}), and the scale vector is at the bottom right of panel (d) and applies to panels (a–d). Vectors smaller than 1/20 (10 kg m^{-1} s^{-1}) of the scale vector are omitted for brevity. These anomalies were estimated from the regression coefficients based on IDX1 in Fig. 5a for each three-pentad mean data. Shaded regions are statistically significant at the 5 % level and are obtained from the correlation coefficients between IDX1 and the precipitation rate anomalies.

anomalies surrounding the Philippines strengthen, and this region with anomalous easterlies extends from the tropical western Pacific to the Indochina Peninsula. The anomalous easterlies correspond to a break in the SCS-SM. An additional anomalous anticyclonic circulation is formed around the Indian subcontinent. Around P31–32 (June 2–7; Figs. 10c, d), anomalous easterlies prevail between 120°E and 160°E in the equatorial Pacific. The positive precipitation rate anomalies zonally increase in the northern part of the anomalous anticyclonic circulation in the western North Pacific (Fig. 10d), although the circulation direction is opposite that of the CCBM (compare Figs. 10a and 10d). An anomalous meridional dipole in precipitation rates is observed in this anomalous anticyclonic circulation, with positive anomalies appearing in the northern part and negative anomalies occurring near the center (Fig. 10d). Figure 8c shows a similar anomalous dipole in early June.

The lifetime of CCBM appears to have the same time scale as ISO. In fact, closed CCBM circulation appears for approximately four pentads (20 days) from P27 to P30 (May 13–28, using the middle days of pentads) (Figs. 9c, d, 10a, b). The anomalous

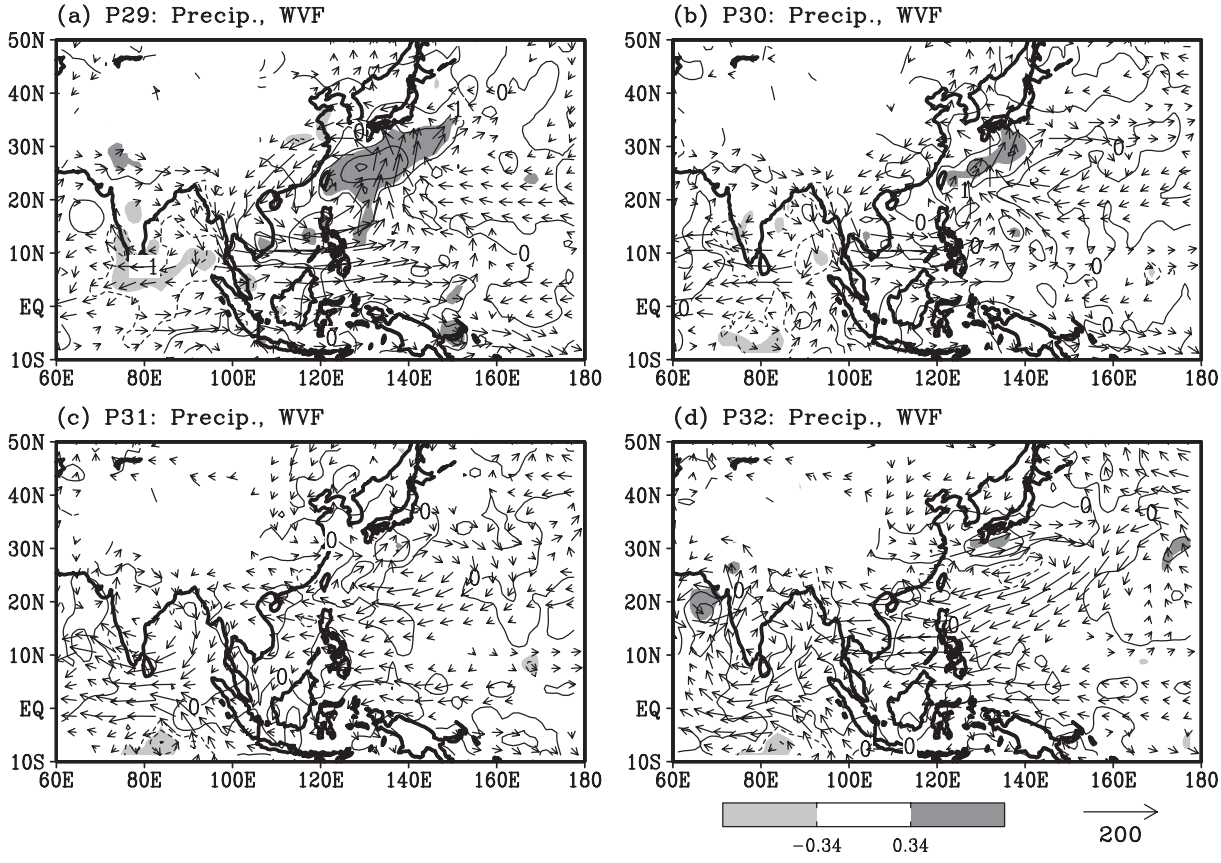

Fig. 10. Similar to Fig. 9 but for the decaying period of the anomalous circulations that control the Baiu frontal activity in May (BFA-M) between P29 and P32, i.e., (a) P29 (May 23), (b) P30 (May 28), (c) P31 (June 2), and (d) P32 (June 7).

southerlies and positive precipitation rate anomalies south of Japan remain for approximately six pentads (30 days) in May (Figs. 8c, 9, 10a, b). We may further observe an ISO cycle with a period of approximately 40 days in the differential precipitation rate anomalies between 20°N and 30°N from May 5 to June 15 (Fig. 8c). The positive precipitation rate anomalies and anomalous zonal wind confluence in the western equatorial Pacific, which occur just before the CCBM is established (Figs. 9a–c), are likely fundamental to CCBM formation.

To identify ISO signals at the equator, this study diagnoses equatorial (10°S–10°N) longitude–time cross sections of the zonal wind anomalies at 850 hPa (U850), the precipitation rate (Fig. 11a), the 30–60 day band-pass filtered OLR, and the vertical p-velocity at 700 hPa (ω700) as representatives of convective activity (Fig. 11b). Positive precipitation rate anomalies corresponding to anomalous latent heating are observed near the eastern edge of the region with anomalous westerlies (Fig. 11a), which move eastward in a stepwise fashion from April to May. In particular, a large stepwise eastward shift from 100°E to 130°E is noticeable in late April. The positive precipitation rate anomalies stay in 130–140°E for half a month in early May. Then, the region with positive precipitation rate anomalies again extends eastward in late May. In June, anomalous easterlies (dashed contours) prevail throughout the entire equatorial region from the Indian Ocean to the western Pacific following the period of anomalous westerlies (solid contours) in May. We estimate a dominant intraseasonal periodicity of approximately 45 days based on the appearance of negative U850 anomalies from 100°E to 120°E.

To discern convective disturbances of the equatorial ISO, we applied the Lanczos band-pass filter (Duchon 1979) with 30–60 day periods to OLR and ω700 (Fig. 11b). We observe the smoothed eastward propagation

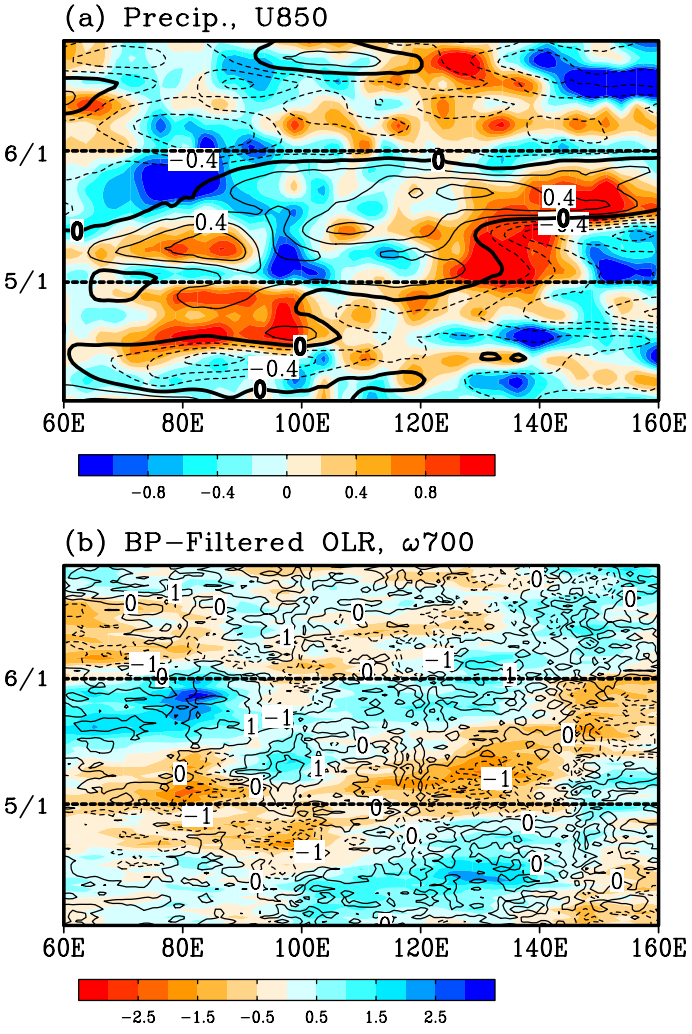

Fig. 11. Time–longitude cross sections of (a) precipitation rate (shade; mm day^{-1}) and U850 (contour; m s^{-1}) anomalies and of (b) band-pass filtered (with an intraseasonal period range of 30–60 days) OLR (shade; W m^{-2}) and ω700 (contour; hPa day^{-1}) anomalies for April to June in the equatorial region (10°S–10°N), which were estimated from the mean of all positive cases in IDX1 (Fig. 5a). Negative anomalies were reproduced with opposite signs. In (a), the shading scale for the precipitation rate anomalies is at the bottom. The contour interval is 0.2 m s^{-1} for U850, and the solid (dashed) contours indicate the positive (negative) anomalies, in which the thick solid contours denote 0 m s^{-1}. In (b), the shading scale for OLR is at the bottom, in which the negative values with warm colors indicate stronger-than-usual convective activity. For the ω700 anomaly, the contour interval is 1.0 hPa day^{-1} and the solid (dashed) contours denote anomalous downward (upward) motions.

of the equatorial ISO disturbances from the Indian Ocean to the western Pacific, although the stepwise eastward shift is still noticeable near 110°E on May 1. The eastward propagation velocity, which was roughly estimated based on eastward movement from 100°E in late April to 160°E in late May (Fig. 11b), is 60° per 30 days, i.e., approximately 3 m s^{-1}. We performed this estimation based on the averaged fields when BFA-M was strong, which may lead to a smaller speed than the estimation for a specific year, such as 1998 (5 m s^{-1}; Straub et al. 2006). Figure 11 shows that strong convective disturbances within the equatorial ISO from late April to early May were followed by CCBM development and a strong BFA-M. We thus identify the equatorial ISO disturbance appearing in late April in the eastern equatorial Indian Ocean as a BFA-M precursor.

In this study, we refine the spatiotemporal processes connecting the equatorial ISO to CCBM formation and further strengthen the BFA-M by examining band-pass (30–60 days) filtered anomalies of the OLR and vertically (1,000–300 hPa) integrated WVFs (Fig. 12). To facilitate comparison with the results of previous studies, this work employed OLR instead of precipitation rate. Considering the CCBM growth and decay discussed with Figs. 9 and 10, the period of Fig. 12 was set from P25 (May 3) to P30 (May 28). Around P25 (May 3; Fig. 12a), we observe an anomalous zonal wind confluence centered in the SCS. In the Bay of Bengal, the cyclonic circulation of an ISO appears with a stronger-than-usual convection. Concurrently, we confirm an anomalous anticyclonic circulation south of Japan and a weaker-than-usual convection in the northern SCS and the southeastern part of this

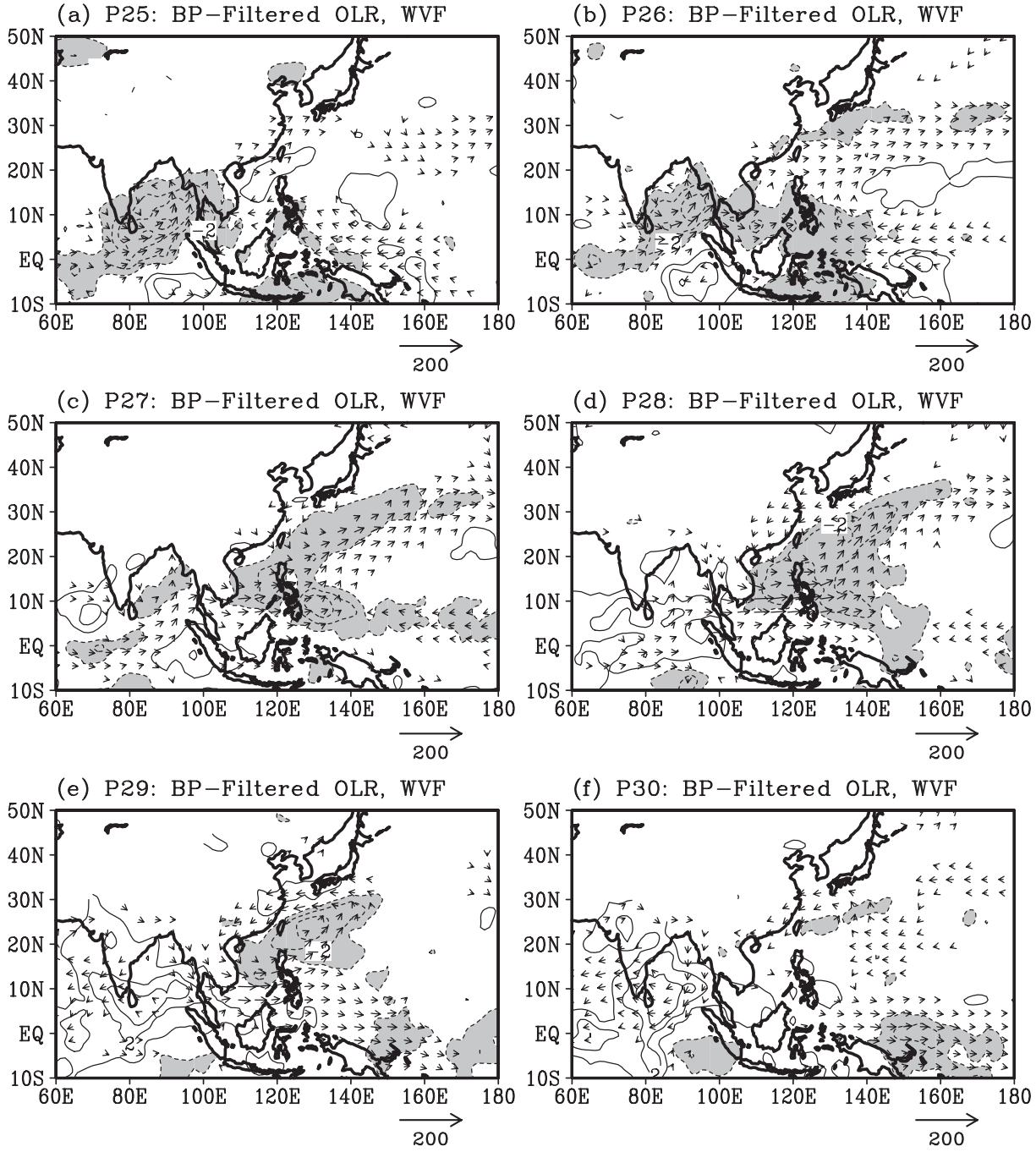

Fig. 12. Band-pass filtered anomalies of OLR (contour; W m^{-2}) and vertically (1,000−300 hPa) integrated WVF (vector; kg m^{-1} s^{-1}) focusing on the intraseasonal time scale of 30−60 days. The distributions were estimated using the regression coefficients based on IDX1 (Fig. 5a). The pentads were set to be (a) P25 (May 3), (b) P26 (May 8), (c) P27 (May 13), (d) P28 (May 18), (e) P29 (May 23), and (f) P30 (May 28) to focus on the lifetime of CCBM (Figs. 9, 10). The contour interval is 1 W m^{-2}, and the dashed (solid) contours exhibit the regions with negative (positive) OLR anomalies indicating stronger-than-usual (weaker-than-usual) convection. The areas with negative OLR anomalies less than −1 W m^{-2} are shaded. The contours of zero are omitted. The scale vector is at the bottom right of each panel. Vectors smaller than 1/20 the size of the scale vector are not drawn for brevity.

anomalous anticyclonic circulation.

By P26 (May 8; Fig. 12b), the confluence region moved eastward to 120°E with an eastward extension of stronger-than-usual convection east of the Philippines. At this time, anomalous southerlies prevailed to the north of this confluence region and then turned northeastward at 20–30°N in the western North Pacific. These southerly wind anomalies affect the activation of BFA-M. In fact, we observe a zonally extending region with stronger-than-usual convection just south of Japan. It is also suggested that SCS-SM onset occurred around this time because of anomalous westerlies with stronger-than-usual convection in the southern SCS, although by definition SCS-SM onset requires additional conditions (Wang et al. 2004).

By P27 (May 13; Fig. 12c), the confluence region shifted farther eastward to 140°E and the zonal band with stronger-than-usual convection extending near the equator moved northward by approximately 5°. Meanwhile, the region with negative OLR anomalies extended northeastward in the western North Pacific. It is notable that stronger-than-usual convection locally developed east of Mindanao in the Philippines by this stage. Around P28 (May 18; Fig. 12d), we observe development of an anomalous large-scale cyclonic circulation, i.e., CCBM, centered at (120°E, 20°N) near Taiwan. This development seems to be a Rossby-type response to convective heating near Mindanao, which further enhances convective activity around Luzon. Focusing on SCS-SM onset in May, Tong et al. (2009) and Wang et al. (2018) have also discussed similar development processes.

The CCBM is weakened during P29–30 (May 23–28; Figs. 12e, f), when the region with an anomalous zonal wind confluence further moves eastward or disappears. Concurrently, convective activity east of the Philippines weakens and the region with stronger-than-usual convection extends in the western equatorial Pacific. In the Indian Ocean, anomalous easterlies prevail on the region with weaker-than-usual convection. During this period, we observe an eastward shift of an anomalous zonal wind divergence from the Bay of Bengal to the SCS. Thus, the ISO in May, which propagates eastward in the tropical Indian and Pacific Oceans, forms the CCBM and strengthens BFA-M with southward expansion.

Several studies (e.g., Lau and Chan 1986; Wang and Xie 1997; Hsu and Weng 2001) have revealed that the coupled Kelvin–Rossby wave packet of the boreal summer ISO could radiate the moist Rossby wave northwestward in the western tropical Pacific. However, these studies have not investigated the interannual variability of BFA-M controlled by ISO activity in May that can modulate SCS-SM onset. In Section 5 we further discuss the connectivity of interannual BFA anomalies from May to June, focusing on the development of anomalous cyclonic and anticyclonic circulations south of Japan that are induced with equatorial ISO disturbances in the western Pacific (Figs. 11, 12).

5. Connectivity from May to June in interannual BFA variability

Interannual BFA variability in June is a spatiotemporal complex with three components (YT11): (1) the biennial component in the western part, (2) the ENSO forcing component in the central part, which has an approximately 4-year cycle period, and (3) the 6-year cycle period component in the eastern part that is remotely forced by the summertime North Atlantic Oscillation. YT11 further demonstrated that the anomalous anticyclonic circulation that appeared south of Japan (see their Fig. 7a) forced the western biennial component of the BFA in June. In this study, we hypothesize that this western biennial component in June is connected with a counterpart in May through the ISO phase reversal in the western tropical Pacific. In fact, between the IDX1 time series of May of this study (Fig. 5a) and YT11's Western Baiu index of June, the correlation coefficient is large (0.41; Table 1) and is statistically significant at the 5 % level (±0.34, d.f. = 34). Additionally, both time series show dominant biennial tendencies (Fig. 5b and YT11's Fig. 3a). Thus, it would be reasonable to hypothesize that a strong connectivity exists between the interannual variabilities of May and of June through a common biennial tendency.

Figure 13 demonstrates a cross-verification of the connectivity between the interannual variabilities of May and June. For the precipitation rate and vertically (1,000–300 hPa) integrated WVF, Fig. 13a shows anomaly fields estimated from regression coefficients in June (P31–35; June 2–22) lagged from the May IDX1 (Fig. 5a). In contrast, Fig. 13b displays the anomaly fields in prior May (P27–30; May 13–28) regressed from the June Western Baiu index of YT11. In Fig. 13a, a region with significant positive precipitation rate anomalies appears in the western part of the BF in June along with an anomalous anticyclonic circulation to the southeast centered at 140°E, 28°N. These features are similar to those shown in Fig. 10d. The negative precipitation rate anomalies in the region of 140–170°E, 5°S–10°N in the western Pacific imply that the convective ISO disturbances were weaker-than-usual in this region. Previous studies have

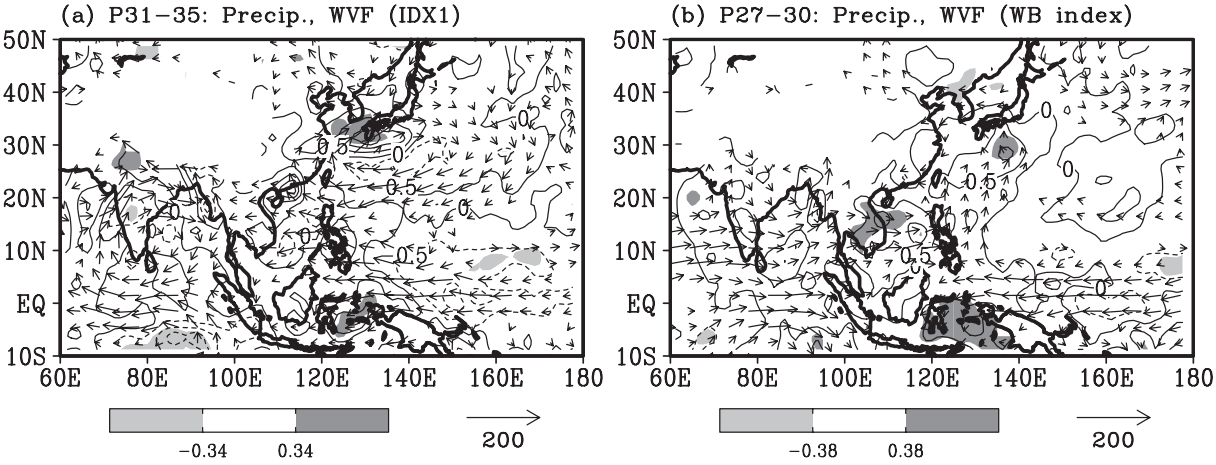

Fig. 13. (a) Lagged regression coefficients of the precipitation rate (contour; mm day^{-1}) and vertically (1,000−300 hPa) integrated WVF (vector; kg m^{-1} s^{-1}) in June, i.e., P31−35 (June 2−22) estimated from IDX1 in May. (b) The counterpart in May, i.e., P27−30 (May 13−28) estimated from the Western Baiu index in June (YT11's Fig. 3a). The contour interval is 0.5 mm day^{-1} and the solid (dashed) contours indicate regions with (positive) negative precipitation rate anomalies. The scale vector is at the bottom right of each panel. Vectors smaller than 1/20 of the scale vector are omitted for brevity. Shading indicates regions that are statistically significant at the 5 % level, which were estimated from the lagged correlation with precipitation rate anomalies, i.e., ±0.34 (d.f. = 34) in (a) and ±0.38 (d.f. = 27) in (b), whose scale is at the bottom of each panel.

suggested that a Rossby-type response could induce such anomalous circulation south of Japan (cf. Wang and Xie 1997; Hsu and Weng 2001). The appearance of similar anomalous anticyclonic circulation was also reported in YT11 (see their Fig. 7a).

YT11's Western Baiu index for June can reproduce the anomaly fields in May that are associated with the interannual variability of BFA-M. Figure 13b displays anomaly fields similar to those shown in Figs. 9c and 12c that is, anomalous southerlies in the Philippine Sea, positive precipitation rate anomalies in the southern half of the BF in May (120−140°E, 20−32°N), and anomalous westerlies (easterlies) in the eastern equatorial Indian Ocean (western equatorial Pacific). Thus, through the ISO phase reversal in the western tropical-subtropical Pacific, interannual BFA-M anomalies are followed by anomalies associated with the interannual variability of YT11's Western Baiu index of June. Note that the ISO phase is opposite between May and June in the western tropical-subtropical Pacific, but ISO disturbances in both phases can strengthen the BFA in May and early June through anomalous circulations with opposite directions (Figs. 10a, d). That is, the BFA in mid-May is strengthened by anomalous southerlies, whereas the anomalous westerlies or southwesterlies enhance the BFA in early June.

The BFA of June in the central part of the BF, which is represented by the Central Baiu index in Table 1, demonstrates the outstanding interannual variability associated with ENSO with a 3−4 year cycle period (YT11; Tomita et al. 2011; YT14; among others). The June IDX2 has a significantly large positive correlation with YT11's Central Baiu index for June (0.82; Table 1). In fact, the preceding wintertime SSTAs associated with the June IDX2 extend like a typical pattern of warm ENSO events (Fig. 7b). In Fig. 14, we diagnosed the anomaly fields in May that preceded those in June associated with IDX2 (Fig. 6b) and with YT11's Central Baiu index for June, that is, the connectivity between May and June in the interannual variability of BFA mainly related to ENSO. In other words, whether the connectivity between the anomaly fields shown in Figs. 6a and 6b is strong.

In May, prior to the cases when the IDX2 of June is positively large (Fig. 6b), regions with negative precipitation rate anomalies extend in the western equatorial Pacific and from the Bay of Bengal to the Philippine Sea through the SCS (Fig. 14a). A similar distribution made based on the YT11's Central Baiu index of June is also confirmed in Fig. 14b. This similarity is ensured by a large positive correlation coefficient between them (0.82; Table 1). The negative precipitation rate anomalies in the Philippine Sea

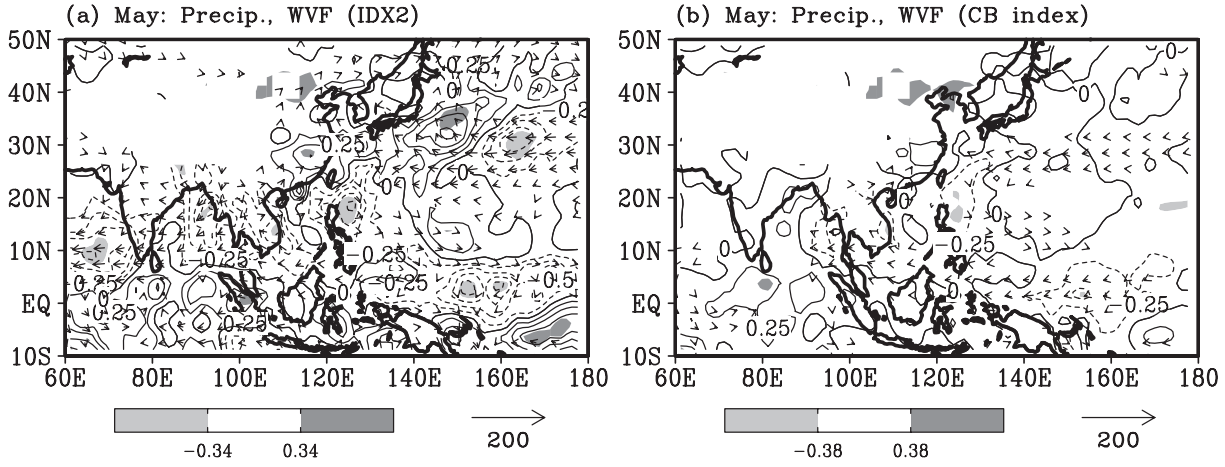

Fig. 14. (a) Lagged regression coefficients of precipitation rate (contour; mm day^{-1}) and vertically (1,000–300 hPa) integrated WVF (vector; kg m^{-1} s^{-1}) in May estimated from the IDX2 of June (Fig. 5a). (b) Like those in May estimated from the Central Baiu index of June (Fig. 3b of YT11). The contour interval is 0.25 mm day^{-1}, and the solid (dashed) contours indicate regions with (positive) negative values. The scale vector is at the bottom right of each panel. Vectors smaller than 1/20 of the scale vector are omitted for brevity. Shading indicates regions that are statistically significant at the 5 % level, which were estimated from the lagged correlation with precipitation rate, i.e., ±0.34 (d.f. = 34) in (a) and ±0.38 (d.f. = 27) in (b), whose scale is at the bottom of each panel.

may correspond to a weaker-than-usual BFA-M in the southern part of the BF (cf. Fig. 2a). Tomita et al. (2010) reported that anomalous Baiu precipitation rate tended to change polarity from May to June following wintertime ENSO events. That is, the BFA-M tends to be weak after warm ENSO events, whereas in the following June the BFA is stronger than usual in the central part of the BF. It is conceivable that the connectivity between the anomaly fields shown in Figs. 6a and 6b is not strong as supported by a weak correlation between the IDX1 of May and the IDX2 of June (0.13; Fig. 5a).

Tomita and Yasunari (1996) and Tomita et al. (2004) revealed that significant signals of tropical biennial oscillation in the ENSO/monsoon system tend to appear in and around the western tropical Pacific. As a key process in the physical mechanisms, they proposed the tropical-extratropical interaction predominant along the eastern edge of the Asian continent from winter to spring. It is suggested that the tropical biennial oscillation may further control the biennial tendency in the springtime ISO activity. To identify the large-scale environment associated with the biennial variability of the springtime ISO, we examined the seasonal mean anomaly fields of March, April, and May (MAM) in the tropical Indian and Pacific Oceans with respect to SST, zonal wind at 300 hPa (U300), vertical wind shear in zonal winds (U300−U700, where U700 denotes zonal wind at 700 hPa), and WVF in the planetary boundary layer (1,000–850 hPa) (Fig. 15). Because IDX1 has a predominant biennial tendency (Fig. 5b), and to focus on its biennial variability, we applied a biennial filter prior to the composite analysis. The seasonal mean anomalies of MAM were estimated from the differential anomalies based on ±0.5σ of the biennial IDX1 in May (positive – negative).

Figure 15a shows the anomaly fields of SST and planetary boundary layer WVF. In the western tropical Pacific, significant negative SSTAs are distributed near the International Date Line with a wedge shape, and positive SSTAs surround this region in a horseshoe pattern. The positive SSTAs are statistically significant around (180°, 20°N) and in the Arafura and Coral Seas that extend to the northeast of Australia. The distribution of SSTAs throughout the entire tropical Pacific is characterized by a tripole pattern, i.e., positive, negative, and positive SSTAs from the west, which resembles the pattern of the ENSO Modoki (Table 1; Ashok et al. 2007). From Fig. 15a we estimate that equatorial SSTs largely decrease eastward in the western tropical Pacific, which effectively disintegrates the equatorial Kelvin–Rossby wave packet there (cf. Wang and Xie 1997). Additionally, SSTAs in the tropical Indian Ocean are nearly zero.

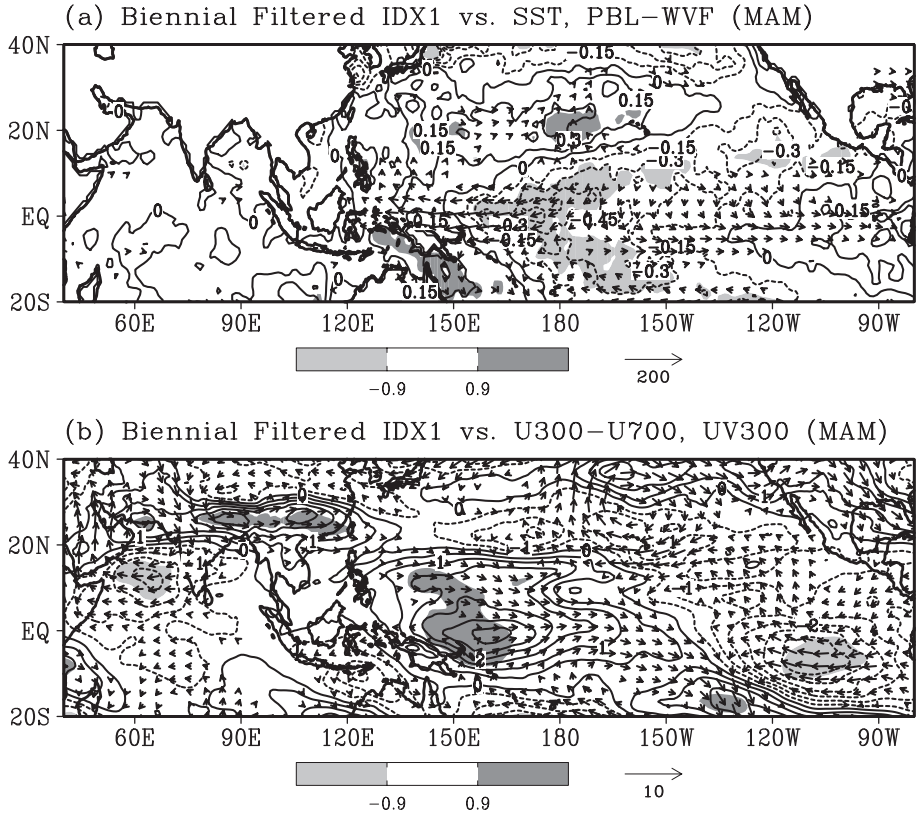

Fig. 15. (a) Anomalies of SST (contour; K) and of WVF in the planetary boundary layer (vector; 1,000−850 hPa; kg m^{-1} s^{-1}) in boreal spring (March, April, and May), which were estimated from the differences between the positive and negative means (positive–negative) for cases exceeding $|\pm 0.5\sigma|$ the biennial IDX1. The contour interval is 0.15 K, and dashed contours indicate regions with negative SSTAs. Shading denotes regions that are statistically significant at the 10 % level, which were estimated from Weltch's two tailed *t*-test for the difference between the two SSTA means. The shading scale and scale vector are at the bottom of (a). Panel (b) is similar to (a), but represents the anomalous environment in the free atmosphere over the planetary boundary layer, i.e., the vertical difference in zonal wind between 700 and 300 hPa (contour; U300−U700; m s^{-1}), and the upper tropospheric horizontal wind at 300 hPa (vector; UV300; m s^{-1}), in which vectors smaller than 1/20 of the scale vector are omitted for brevity. Statistical significance was tested with methods similar to (a), but were based on the vertical difference in the zonal winds.

Near-surface easterlies are anomalously prevailing in the western equatorial Pacific, where SSTAs change the polarities from positive to negative from the west. A large-scale divergence is then formed around (170°W, 0°) concurrently with the anomalous near-surface westerlies in the eastern equatorial Pacific. The anomalous easterlies in the western equatorial Pacific that traverse the SSTA isotherms induce lower-temperature advection from the east, which may further enhance near-surface static instability over positive SSTA regions. Because the vectors are estimated from the flow of water vapor in the planetary boundary layer, the anomalous easterlies may cause convective instability that induces the anomalous ascent of Walker circulation near the Indonesian maritime continent. Lower-tropospheric static and convective instabilities effectively reinforce the convective activity, including ISO disturbances on the western edge of the equatorial Pacific, which is then followed by CCBM formation (Figs. 6a, 9d, 12d).

A moist Rossby wave, which separates from the equatorial Kelvin–Rossby wave packet of well-organized ISO disturbances, tends to propagate northwestward in the region with an easterly vertical shear (Xie and Wang 1996; Wang and Xie 1997; Jiang et al. 2004; Deng and Li 2016). Figure 15b shows the hor-

izontal wind anomalies at 300 hPa (UV300; vector) and vertical differences in zonal winds between 700 and 300 hPa (U300 - U700; contour). A region with anomalous westerly vertical shear appears in the western tropical Pacific, which is probably formed by the enhanced Walker circulation with the La Niña Modoki (Ashok et al. 2007). In fact, we observe anomalous easterlies (westerlies) in the lower (upper) troposphere in the western tropical Pacific (Figs. 15a, b). The SSTA and anomalous westerly vertical shear fields extending in the western tropical Pacific (Figs. 15a, b) are suitable for disintegrating the equatorial Kelvin–Rossby wave packet there and for confining the northwestward propagation of the moist Rossby wave. Additionally, an anomalous region with significant westerlies and westerly vertical shear appears along 25°N just south of the Tibetan Plateau.

6. Summary

The BF is climatologically formed in May in the western North Pacific and BFA-M has specific interannual variability. This study investigated the characteristics and physical processes of the interannual variability of BFA-M and discussed its connectivity with June. To approach these issues, objective ERA-Interim data from 1979 to 2014 (36 years) were diagnosed. Additionally, we examined the NOAA OLR and GPCP precipitation rate datasets. The diagnostic techniques used in this study were composite, regression, and correlation analyses. A cluster analysis was also employed to diagnose connectivity between interannual variabilities in May and June. To extract the ISO components and emphasize the biennial tendency, this study used band-pass and high-pass filters considering the temporal resolution of data (i.e., daily or yearly).

The BF is established in May in the western North Pacific when the large-scale updraft is enhanced there. This is dynamically induced by positive temperature advection in the middle troposphere with warm moist southerlies from the tropics (Fig. 1). In May, the BF first widens southward and then moves northward while narrowing its north-south width during June (Fig. 3). The seasonal development of local Hadley circulation leads to a northward shift of the BF through the northwestward extension of the subtropical high in the western North Pacific (Fig. 2). The BFA has a large interannual standard deviation in the region where Baiu precipitation rate is climatologically large (Figs. 2, 3).

Anomalous meridional winds in the eastern part of the CCBM centered at Taiwan control the interannual variability of BFA-M (Figs. 6a, 9, 10, 12). The CCBM is likely to be forced as a moist Rossby wave that separated from the equatorial Kelvin–Rossby wave packet in the western tropical Pacific, i.e., the springtime equatorial ISO that propagates eastward from the Indian Ocean to the western Pacific (Wang and Xie 1997; Hsu and Weng 2001). The CCBM is also probably related to SCS-SM onset (Chan et al. 2002; Tong et al. 2009; Wang et al. 2018), although the observed correlation was somewhat weak (Table 1). Tong et al. (2009) further identified that a midlatitude front tends to move southward just after SCS-SM onset, which may correspond to the reinforcement of BFA and southward expansion of BF in May when the CCBM is anomalously enhanced. This suggests that ISO signals in the equatorial Indian Ocean in April can be a precursor to following CCBM development and reinforcement of BFA-M (Fig. 11).

In early June, almost opposite anomaly fields appear with the out-of-phase ISO in the western tropical Pacific, inducing anomalous anticyclonic circulation south of Japan (Fig. 10). The anomalous southwesterlies in the northwestern part of this anticyclonic circulation then increase the precipitation rate in the western part of the BF (Fig. 10d). Interestingly, the direction of anomalous large-scale circulation in the western North Pacific reverses between May and early June, but a continuous increase of Baiu precipitation rate appears for the two periods (Figs. 10a, d). The BFA-M can have a positive lag correlation with the early June BFA evaluated by YT11 as the Western Baiu (Table 1); therefore, the BFA-M can be a predictor of the western BFA in June.

The interannual modulation of May ISO activity in the western North Pacific is a key for the biennial BFA-M tendency. To evaluate its interannual modulation, the associated background springtime environment was investigated (Fig. 15). The SSTA distribution shows a tripole pattern in the tropical Pacific similar to that of the ENSO Modoki (Table 1, Fig. 15a). The anomalously forced Walker circulation can modify vertical zonal wind shear in the western tropical Pacific (Fig. 15b). The zonal SSTA gradient and modified vertical zonal wind shear in the western tropical Pacific are both favorable to confining the location of strong ISO activity (Wang and Xie 1997). For example, in the winters of the La Niña Modoki, ISO activity is very strong in the western tropical Pacific and around the Indonesian maritime continent (Feng et al. 2015; Pang et al. 2016). In contrast, in El Niño winters, ISO activity tends to be strong to the east of the International Date Line but weak around

the Indonesian maritime continent (Liu et al. 2016; Pang et al. 2016). These results are consistent with the findings of this study, although the season differs. Such a background environment may effectively confine May ISO activity to the tropical western North Pacific.

Interannual modulations of the June and July BFA are predominantly ENSO-driven (Tomita et al. 2010, YT11, YT14). The interannual BFA anomalies are forced with an elliptical anomalous circulation extending along the BF to the south of Japan during these months (Fig. 6b), and the anomalies are maintained during the two months with the same polarity, with the polarity being opposite in May (Fig. 14; Tomita et al. 2010). The ENSO-forced interannual BFA-M anomalies may be small and less organized than those forced by the biennial ENSO Modoki with the modulation of springtime ISO activity (compare Figs. 6a and 14a). Thus, the biennial component of the interannual BFA-M anomalies could be dominant in May (Fig. 5a). The effects of biennial springtime ISO forcing can locally survive in the western part of the BF in June (YT11) but disappear by July (YT14).

Lastly, we should note that two important questions remain. The first is what mechanisms adjust the timing of the springtime ISO into May, and the second is why the timing adjustment has a biennial tendency. Regarding the first question, Wang and Xie (1997) suggested that the cycle period of boreal summer ISO could be determined by the westward propagation of off-equatorial Rossby waves emanating from the tropical western North Pacific. Therefore, the location where the off-equatorial Rossby waves of boreal summer ISO were emanated may be a factor controlling the timing (cf. Fig. 15). Additionally, Wang and Xu (1997) showed that SCS-SM onset, which sometimes occurs with springtime ISO development (cf. Fig. 9), certainly had a singularity around P28 (May 18). Regarding this singularity, they speculated that it was determined by the nonlinear relationship of the seasonal march of planetary-scale circulation systems with surface sensible heat flux of either the Philippines or the Indonesian maritime continent. This study implies that this singularity is not perfectly locked, but rather is unlocked biennially.

The physical mechanisms of the tropospheric biennial oscillation of the ENSO/monsoon system have been studied by many researchers (e.g., Tomita and Yasunari 1996; Meehl 1997; Chang and Li 2000). Recently, Son et al. (2017) further demonstrated that the stratospheric quasi-biennial oscillation could modulate the boreal winter ISO in the tropical Indian and Pacific Oceans. For a more complete understanding of how the anomalous interannual environment modulates springtime ISO activity in the tropical Indian and Pacific Oceans, further study will be required to elucidate the more detailed physical mechanisms.

Acknowledgments

This study was partly supported by the fund of Cooperative Research Program of the "Network Joint Research Center for Materials and Devices" and by Grant-in-Aid for Challenging Exploratory Research (19K22876) of Japan Society for the Promotion of Science.

References

Adler, R. F., G. J. Huffman, A. Chang, R. Ferraro, P.-P. Xie, J. Janowiak, B. Rudolf, U. Schneider, S. Curtis, D. Blovin, A. Gruber, J. Susskind, P. Arkin, and E. Nelkin, 2003: The version-2 Global Precipitation Climatology Project (GPCP) monthly precipitation analysis (1979–present). *J. Hydrometeor.*, **4**, 1147–1167.

Ashok, K., S. K. Behera, S. A. Rao, H. Weng, and T. Yamagata, 2007: El Niño Modoki and its possible teleconnection. *J. Geophys. Res.*, **112**, C11007, doi:10.1029/2006JC003798.

Chan, J. C. L., W. Ai, and J. Xu, 2002: Mechanisms responsible for the maintenance of the 1998 South China Sea summer monsoon. *J. Meteor. Soc. Japan*, **80**, 1103–1113.

Chang, C.-P., and T. Li, 2000: A theory for the tropical tropospheric biennial oscillation. *J. Atmos. Sci.*, **57**, 2209–2224.

Chen, T.-C., M.-C. Yen, and S.-P. Weng, 2000: Interaction between the summer monsoons in East Asia and the South China Sea: Intraseasonal monsoon modes. *J. Atmos. Sci.*, **57**, 1373–1392.

Dee, D. P., S. M. Uppala, A. J. Simmons, P. Berrisford, P. Poli, S. Kobayashi, U. Andrae, M. A. Balmaseda, G. Balsamo, P. Bauer, P. Bechtold, A. C. M. Beljaars, L. van de Berg, J. Bidlot, N. Bormann, C. Delsol, R. Dragani, M. Fuentes, A. J. Geer, L. Haimberger, S. B. Healy, H. Hersbach, E. V. Hólm, L. Isaksen, P. Kållberg, M. Köhler, M. Matricardi, A. P. McNally, B. M. Monge-Sanz, J.-J. Morcrette, B.-K. Park, C. Peubey, P. de Rosnay, C. Tavolato, J.-N. Thépaut, and F. Vitart, 2011: The ERA-Interim reanalysis: Configuration and performance of the data assimilation system. *Quart. J. Roy. Meteor. Soc.*, **137**, 553–597.

Deng, L., and T. Li, 2016: Relative roles of background moisture and vertical shear in regulating interannual variability of boreal summer intraseasonal oscillations. *J. Climate*, **29**, 7009–7025.

Duchon, C. E., 1979: Lanczos filtering in one and two dimensions. *J. Appl. Meteor.*, **18**, 1016–1022.

Feng, J., P. Liu, W. Chen, and X. Wang, 2015: Contrasting Madden–Julian oscillation activity during various stages of EP and CP El Niños. *Atmos. Sci. Lett.*, **16**, 32–37.

Hsu, H.-H., and C.-H. Weng, 2001: Northwestward propagation of the intraseasonal oscillation in the western North Pacific during the boreal summer: Structure and mechanism. *J. Climate*, **14**, 3834–3850.

Jiang, X., T. Li, and B. Wang, 2004: Structures and mechanisms of the northward propagating boreal summer intraseasonal oscillation. *J. Climate*, **17**, 1022–1039.

Kodama, Y.-M., 1999: Roles of the atmospheric heat sources in maintaining the subtropical convergence zones: An aqua-planet GCM study. *J. Atmos. Sci.*, **56**, 4032–4049.

Kosaka, Y., S.-P. Xie, and H. Nakamura, 2011: Dynamics of interannual variability in summer precipitation over East Asia. *J. Climate*, **24**, 5435–5453.

Lau, K.-M., and P. H. Chan, 1986: Aspects of the 40–50 day oscillation during the northern summer as inferred from outgoing longwave radiation. *Mon. Wea. Rev.*, **114**, 1354–1367.

Lau, K.-M., H.-T. Wu, and S. Yang, 1998: Hydrologic processes associated with the first transition of the Asian summer monsoon: A pilot satellite study. *Bull. Amer. Meteor. Soc.*, **79**, 1871–1882.

Lawrence, D. M., and P. J. Webster, 2002: The boreal summer intraseasonal oscillation: Relationship between northward and eastward movement of convection. *J. Atmos. Sci.*, **59**, 1593–1606.

Liebmann, B., and C. A. Smith, 1996: Description of a complete (interpolated) outgoing longwave radiation dataset. *Bull. Amer. Meteor. Soc.*, **77**, 1275–1277.

Liu, F., T. Li, H. Wang, L. Deng, and Y. Zhang, 2016: Modulation of boreal summer intraseasonal oscillations over the western North Pacific by ENSO. *J. Climate*, **29**, 7189–7201.

Madden, R. A., and P. R. Julian, 1994: Observations of the 40-50-day tropical oscillation—A review. *Mon. Wea. Rev.*, **122**, 814–837.

Mao, J., and J. C. L. Chan, 2005: Intraseasonal variability of the South China Sea summer monsoon. *J. Climate*, **18**, 2388–2402.

Meehl, G. A., 1997: The South Asian monsoon and the tropospheric biennial oscillation. *J. Climate*, **10**, 1921–1943.

Murakami, T., and J. Matsumoto, 1994: Summer monsoon over the Asian continent and western North Pacific. *J. Meteor. Soc. Japan*, **72**, 719–745.

Okada, Y., and K. Yamazaki, 2012: Climatological evolution of the Okinawa Baiu and differences in large-scale features during May and June. *J. Climate*, **25**, 6287–6303.

Pang, B., Z. Chen, Z. Wen, and R. Lu, 2016: Impacts of two types of El Niño on the MJO during boreal winter. *Adv. Atmos. Sci.*, **33**, 979–986.

Rasmusson, E. M., and T. H. Carpenter, 1982: Variations in tropical sea surface temperature and surface wind fields associated with the Southern Oscillation/El Niño. *Mon. Wea. Rev.*, **110**, 354-384.

Sampe, T., and S.-P. Xie, 2010: Large-scale dynamics of the meiyu-baiu rainband: Environmental forcing by the westerly jet. *J. Climate*, **23**, 113–134.

Son, S.-W., Y. Lim, C. Yoo, H. H. Hendon, and J. Kim, 2017: Stratospheric control of the Madden-Julian oscillation. *J. Climate*, **30**, 1909–1922.

Straub, K. H., G. N. Kiladis, and P. E. Ciesielski, 2006: The role of equatorial waves in the onset of the South China Sea summer monsoon and the demise of El Niño during 1998. *Dyn. Atmos. Oceans*, **42**, 216–238.

Tanaka, M., 1997: Interannual and interdecadal variations of the western North Pacific monsoon and Baiu rainfall and their relationship to the ENSO cycles. *J. Meteor. Soc. Japan*, **75**, 1109–1123.

Tomita, T., and T. Yasunari, 1996: Role of the northeast winter monsoon on the biennial oscillation of the ENSO/monsoon system. *J. Meteor. Soc. Japan*, **74**, 399–413.

Tomita, T., T. Yoshikane, and T. Yasunari, 2004: Biennial and lower-frequency variability observed in the early summer climate in the western North Pacific. *J. Climate*, **17**, 4254–4266.

Tomita, T., M. Nonaka, and T. Yamaura, 2010: Interannual variability in the subseasonal northward excursion of the Baiu front. *Int. J. Climatol.*, **30**, 2205–2216.

Tomita, T., T. Yamaura, and T. Hashimoto, 2011: Interannual variability of the Baiu season near Japan evaluated from the equivalent potential temperature. *J. Meteor. Soc. Japan*, **89**, 517–537.

Tong, H. W., J. C. L. Chan, and W. Zhou, 2009: The role of MJO and mid-latitude fronts in the South China Sea summer monsoon onset. *Climate Dyn.*, **33**, 827–841.

Wang, B., and X. Xie, 1997: A model for the boreal summer intraseasonal oscillation. *J. Atmos. Sci.*, **54**, 72–86.

Wang, B., and X. Xu, 1997: Northern Hemisphere summer monsoon singularities and climatological intraseasonal oscillation. *J. Climate*, **10**, 1071–1085.

Wang, B., and LinHo, 2002: Rainy season of the Asian–Pacific summer monsoon. *J. Climate*, **15**, 386–398.

Wang, B., R. Wu, and X. Fu, 2000: Pacific–East Asian teleconnection: How does ENSO affect East Asian climate? *J. Climate*, **13**, 1517–1536.

Wang, B., LinHo, Y. Zhang, and M.-M. Lu, 2004: Definition of South China Sea monsoon onset and commencement of the East Asia summer monsoon. *J. Climate*, **17**, 699–710.

Wang, H., F. Liu, B. Wang, and T. Li, 2018: Effects of intraseasonal oscillation on South China Sea summer monsoon onset. *Climate Dyn.*, **51**, 2543–2558.

Xie, S.-P., K. Hu, J. Hafner, H. Tokinaga, Y. Du, G. Huang, and T. Sampe, 2009: Indian Ocean capacitor effect on Indo-western Pacific climate during the summer

following El Niño. *J. Climate*, **22**, 730–747.

Xie, X., and B. Wang, 1996: Low-frequency equatorial waves in vertically sheared zonal flow. Part II: Unstable waves. *J. Atmos. Sci.*, **53**, 3589–3605.

Yamaura, T., and T. Tomita, 2011: Spatiotemporal differences in the interannual variability of Baiu frontal activity in June. *Int. J. Climatol.*, **31**, 57–71.

Yamaura, T., and T. Tomita, 2014: Two physical mechanisms controlling the interannual variability of Baiu precipitation. *J. Meteor. Soc. Japan*, **92**, 305–325.

Yoshikane, T., F. Kimura, and S. Emori, 2001: Numerical study on the Baiu front genesis by heating contrast between land and ocean. *J. Meteor. Soc. Japan*, **79**, 671–686.